Supplementary Materials for

On-Skin Artificial Intelligence via Supramolecular Polymer Memtransistors

Ngoc Thanh Phuong Vo[1‡], *Eun Joo Yoo*[2‡], *Kyu Ho Jung*[1], *Min Woo Jeong*[1], *Seon Hoo Park*[1],
Thuy An Nguyen[1], *Hye Rin Chang*[1], *Seung Hwan Lee*[2,3*], *Jin Young Oh*[1*]

[1]Department of Chemical Engineering (Integrated Engineering Program), Kyung Hee University, Yongin, Republic of Korea.

[2]Department of Electronics Engineering, Kyung Hee University, Yongin, Gyeonggi 17104, Korea

[3]Department of Semiconductor Engineering, Kyung Hee University, Yongin, Gyeonggi 17104, Korea

[‡]These authors contributed equally to this work

*Corresponding Authors. Email: seulee@khu.ac.kr; jyoh@khu.ac.kr

Table of Contents Summary

Supplementary Notes

Supplementary Note 1. Characteristics of the FETs

The field effect mobility (μ_{FE}) is calculated in saturation regime by fitting the plot of the linear regime of square root of drain current $\sqrt{I_D}$ versus gate voltage (V_G). The equation follows (S1):

$$\mu_{\mathrm{FE}} = \frac{2L}{WC_i}\left(\frac{\partial\sqrt{I_D}}{\partial V_G}\right)^2 \qquad \text{(S1)}$$

where L is the length of the channel, W is width of the channel. C_i is capacitance per unit area of gate dielectric. The values of all parameters with and without tensile strain are shown at Table S1.

Supplementary Note 2. Decay constant (τ) calculation from activation energy.

The activation energy was calculated following the Arrhenius correlation plot with various temperature:[3]

$$\mu \propto \exp(-E_A/kT) \qquad \text{(S2)}$$

where k is the Boltzmann constant and μ values were measured in the linear regime under low drain–source voltage.

The decay constant was calculated from the activation energy with fading memory characteristic is well fitted by the stretched-exponential expression. The equation follows:

$$\tau = \tau_0 \, exp(E_A/(k_B T)) \qquad \text{(S3)}$$

Where τ is time characteristic, E_A is the charge activation energy, k_B is the Boltzmann constant, and T is the ambient temperature

Supplementary Note 3. Schottky current calculation.

The equation for Schottky current calculation follows:

$$I_S = AA * T^2 \exp(-q\emptyset/(k_B\, T)) \qquad \text{(S4)}$$

in which k_B, T, and q are the Boltzmann constant, absolute temperature, and elementary charge, respectively. ϕ is the Schottky barrier height of the interface between pn junction, A is the area of Schottky contact, and $A*$ is the effective Richardson constant. ϕ is obtained by the slope.

Supplementary Note 4. Decay time (τ) calculation from stretched-exponential expression.

The synaptic behavior with fading memory characteristic is well fitted by the stretched-exponential expression. The equation follows:[3]

$$I(t) = I_0 + \Delta I_d \, exp[-((t-t_0)/\tau)^{\beta}] \qquad \text{(S5)}$$

where ΔI_d is responsive current and τ is the temporal characteristic constant, β is inhibitory temporal factor.

Supplementary Note 5. Calculation method for surface energies of the neat DPPT-TT, 3:7 blend film, and neat SPE elastomer.

The surface free energies are calculated using the Owens-Wendt method:[2]

$$\gamma_c = \gamma_c^p + \gamma_c^d \tag{S6}$$

$$(1 + \cos\theta_l)\gamma_l = 2\left(\sqrt{\gamma_l^d \gamma_c^d} + \sqrt{\gamma_l^p \gamma_c^p}\right) \tag{S7}$$

where γ_c, γ_c^p, and $\gamma_c^d$are the total surface energy, polar component and dispersive component of surface energy of testing materials, respectively. Where θ_l, γ_l, γ_l^p, and γ_l^d are the contact angle, total surface energy, polar and dispersive component of surface energy of the test liquid, which are water and diiodomethane. $\gamma_{diiodomethane}$ = 50.8 mJ/m^2, γ_{water} = 72.8 mJ/m^2, γ_{water}^d = 21.8 mJ/m^2 and γ_{water}^p = 51 mJ/m^2.

Supplementary Note 6. Cochleargram.

The cochleargram is a time-frequency representation of audio signals, which mimics the functionality of the human cochlea, which processes sound. This preprocessing method converts raw audio waveforms into a 2D matrix by decomposing the signal into multiple frequency bands over time. It can effectively capture the temporal and spectral features of the sound. In this study, the cochleargram is utilized to extract key features from the AudioMNIST dataset. It enables efficient transformation of audio signals into a format suitable for machine learning. The cochleargram preserves crucial paralinguistic information, such as intonation, pitch and accent, which are critical for tasks like speech and emotion recognition. By digitizing these features into binary spikes, the cochleargram ensures compatibility with the input requirements of neuromorphic systems, bridging the gap between biological inspiration and computational implementation.

Supplementary Note 7. Mel-spectrogram.

The mel-spectrogram is a time-frequency representation that maps the frequency components onto the mel scale. This mel scale is a perceptual scale for pitches designed to imitate how humans perceive sound. It can focus on a linear relationship at lower frequencies and a logarithmic relationship at higher frequencies mimicking the sensitivity of the human auditory system. In the process of mel scaling, a Short-Time Fourier Transform (STFT) captures the frequency content, followed by the application of mel filter banks to map the resulting frequencies onto the mel scale.

In this research, we utilized mel spectrogram to extract features from the RAVDESS. The specific parameters used for mel spectrogram extraction included 100 mel bands, a 2048-point FFT window size, and a frequency range of 50 Hz to 8000 Hz. The resulting spectrograms were then normalized to decibels (dB) for better dynamic range representation and resampled to a fixed target shape of 60×120 to ensure consistency across all samples. To demonstrate that our classification performance derives from the reservoir's intrinsic ability to capture natural temporal properties rather than the specific preprocessing steps, we employed cochleagrams for the AudioMNIST dataset and mel-spectrograms for the RAVDESS dataset.

Supplementary Note 8. Reservoir Contribution to Lorenz Attractor Prediction.

The Lorenz attractor exhibits strong nonlinearity and complexity, making stable prediction using only a fully connected layer challenging. Such time-series data can be encoded via a reservoir, thereby reducing the computational burden on the readout layer while effectively capturing sequential dependencies; as a result, prediction accuracy is enhanced even with a smaller volume of input data processed by the reservoir. The mechanism enabling this is as follows:

We employed a 4-bit reservoir system. For each of the x, y, and z axes, a sliding time window of length 4 was sequentially injected into the reservoir and projected onto the corresponding reservoir state. 49 reservoir states were fed simultaneously into the readout layer, and by incorporating all three axes of the Lorenz attractor, 147 input nodes were processed in a single step. The readout layer then predicted the coordinate at the 50th time step, and this prediction was recursively fed back as input for multi-step-ahead forecasting. However, owing to the chaotic nature of the Lorenz attractor, errors accumulated over time, causing predictions to deviate significantly. To mitigate this issue, we introduced online training.

Supplementary Figures

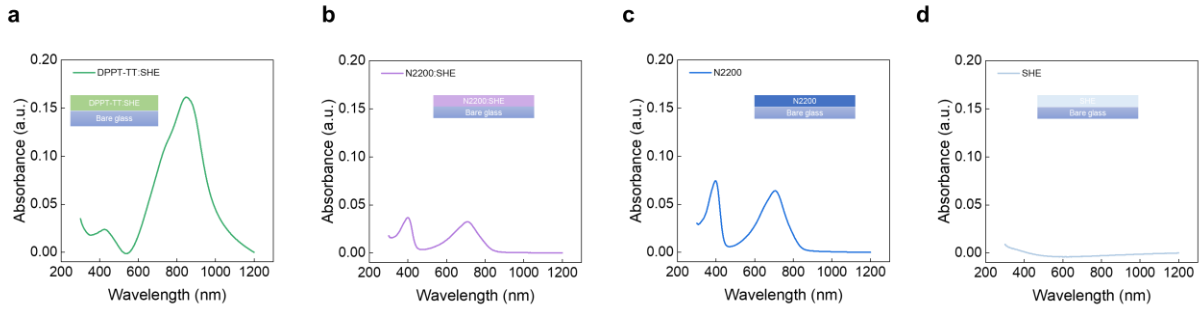

Supplementary Fig. 1. UV-Vis spectra of **a,** blend p-type, **b,** blend n-type, **c,** pure n-type semiconducting layers, and **d,** pure SPE layer.

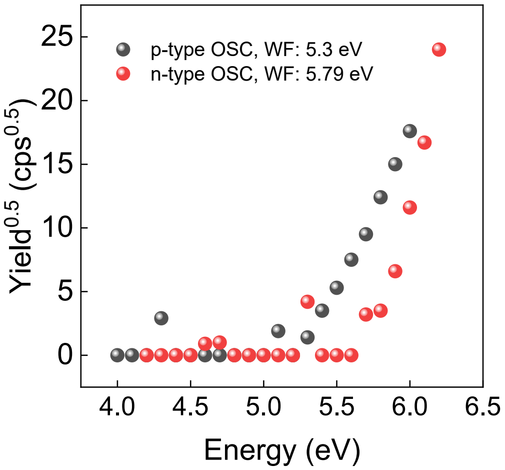

Supplementary Fig. 2. Work functions of p-type OSC and n-type OSC using PESA measurement.

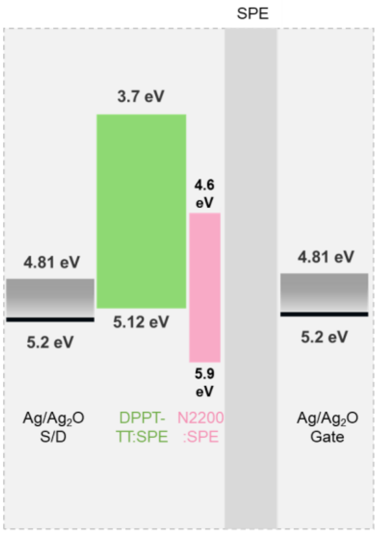

Supplementary Fig. 3. Schematic of energy-level alignment at the p-n heterojunction.

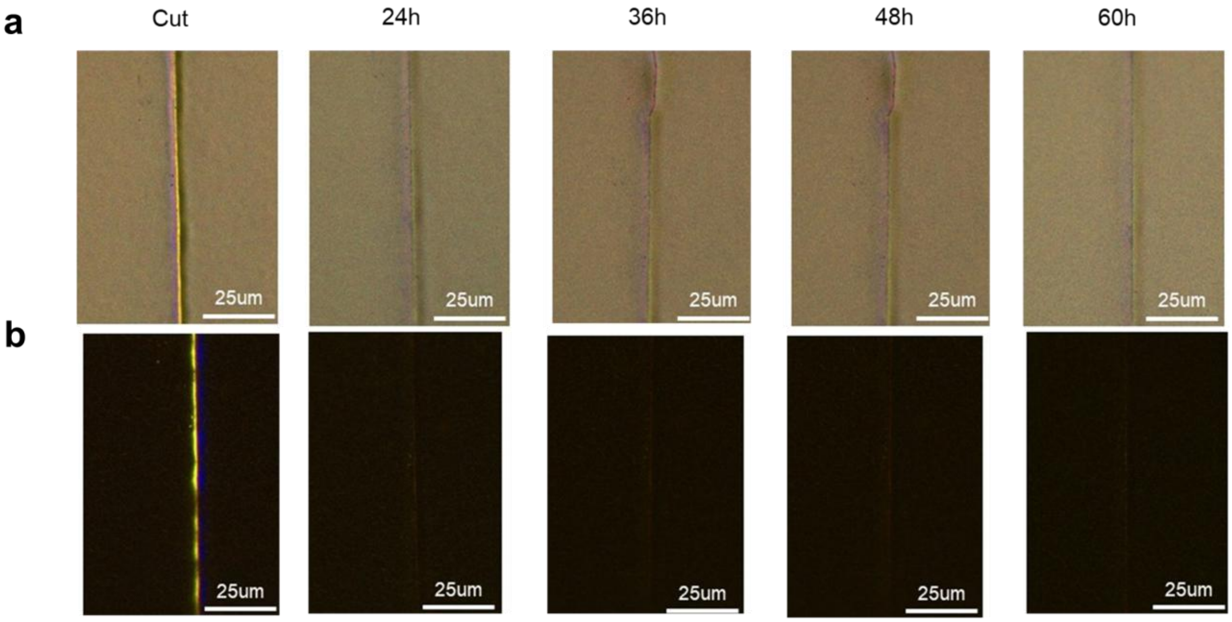

Supplementary Fig. 4. OM images of gate electrode with tracking healing time. The images is taken in **a,** bright and **b,** dark field mode.

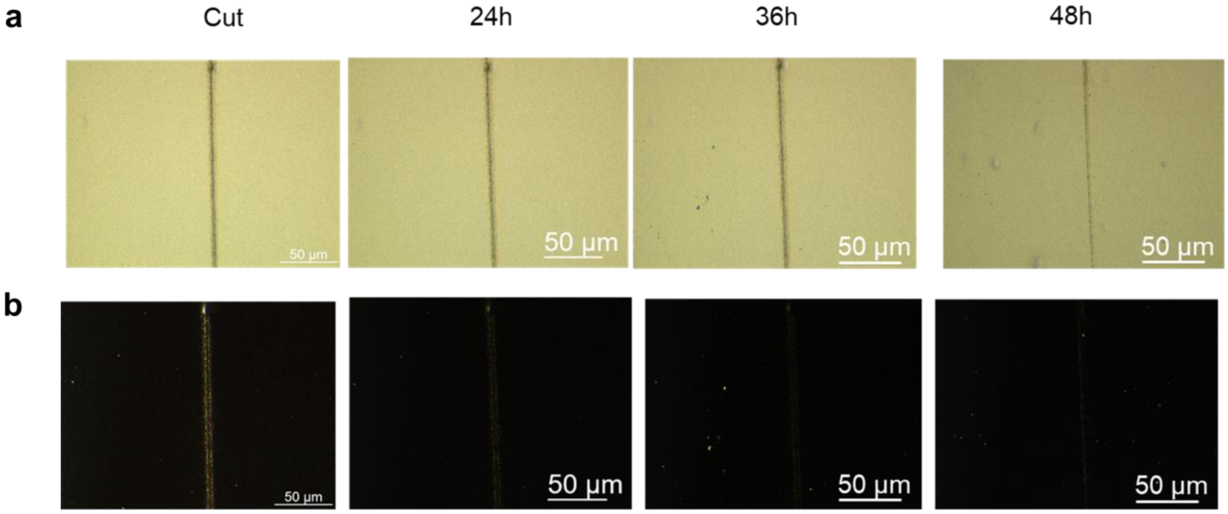

Supplementary Fig. 5. OM images of S/D electrode under 3 μm cutting with tracking healing time. The images is taken in **a,** bright and **b,** dark field mode.

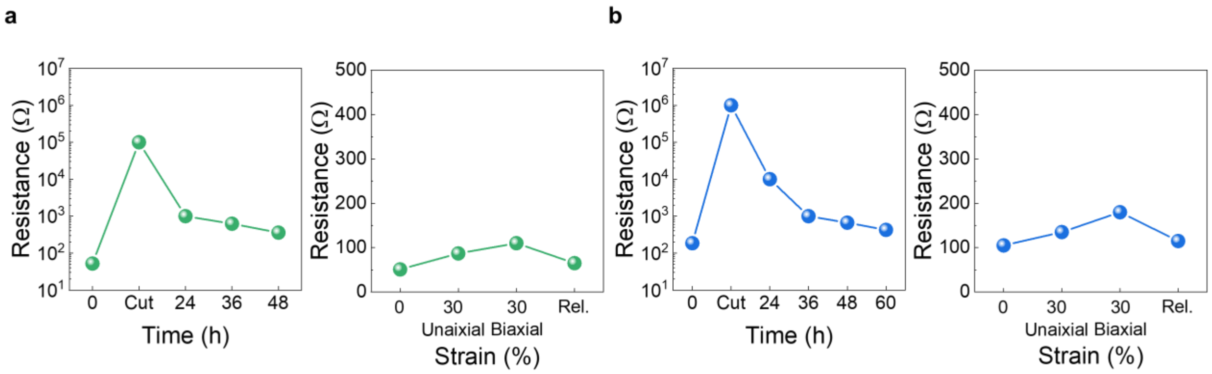

Supplementary Fig. 6. Resistance change of **a,** source/drain (S/D) and **b,** gate electrode during tracking stretching and healing time.

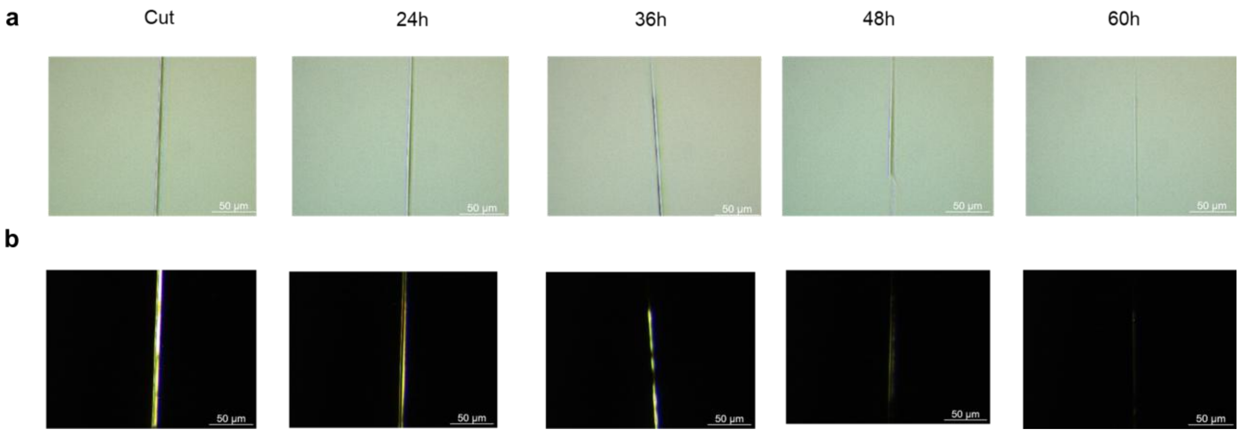

Supplementary Fig. 7. OM images of dielectric under 3 μm cutting with tracking healing time. The images is taken in **a,** bright and **b,** dark field mode.

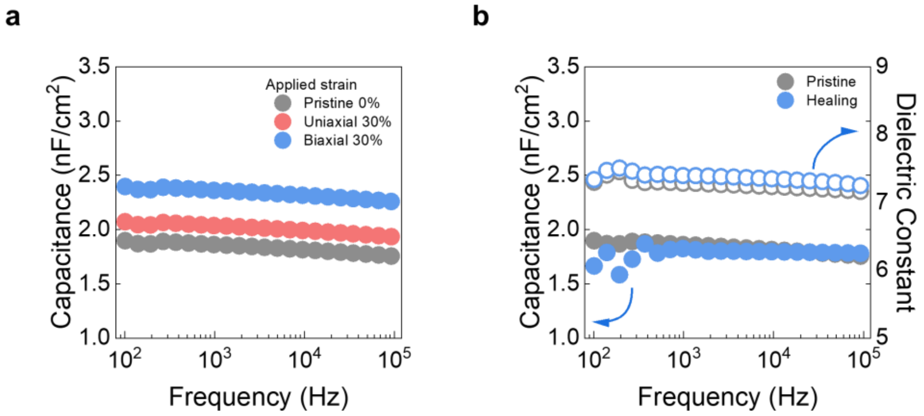

Supplementary Fig. 8. Capacitance and k value of self-healing dielectric under **a,** stretching and **b,** healed conditions.

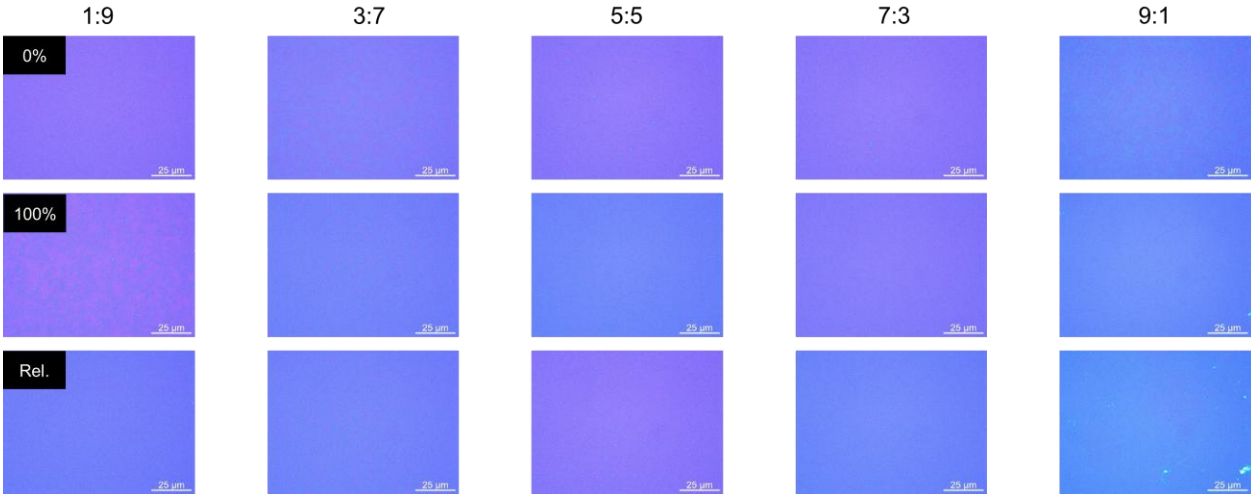

Supplementary Fig. 9. OM images of N2200:SPE blending films with various blending ratios under 0% (top), 100% (middle), and release (bottom).

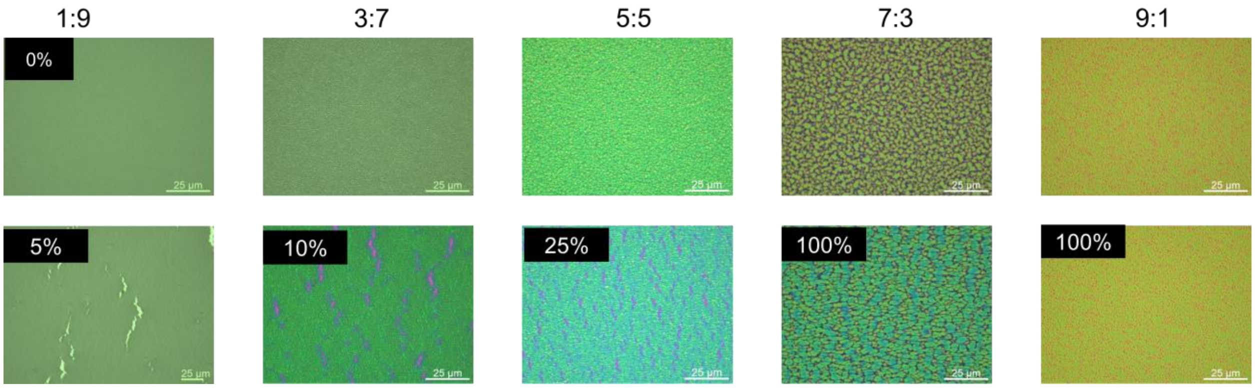

Supplementary Fig. 10. OM images of DPPT-TT:SPE blending films with various blending ratios.

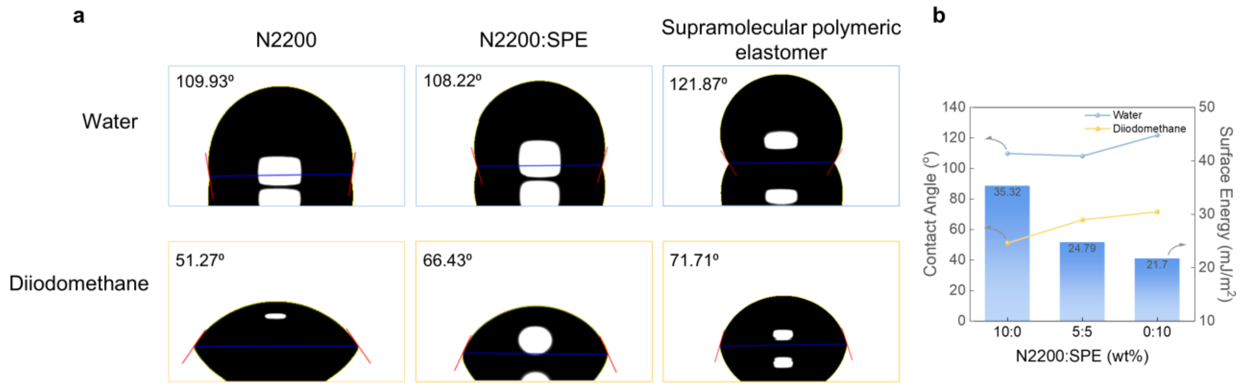

Supplementary Fig. 11. a, Optical image showing the contact angles of the N2200, 5:5 blending film and supramolecular polymeric elastomer. **b,** The surface energies and contact angles of different films.

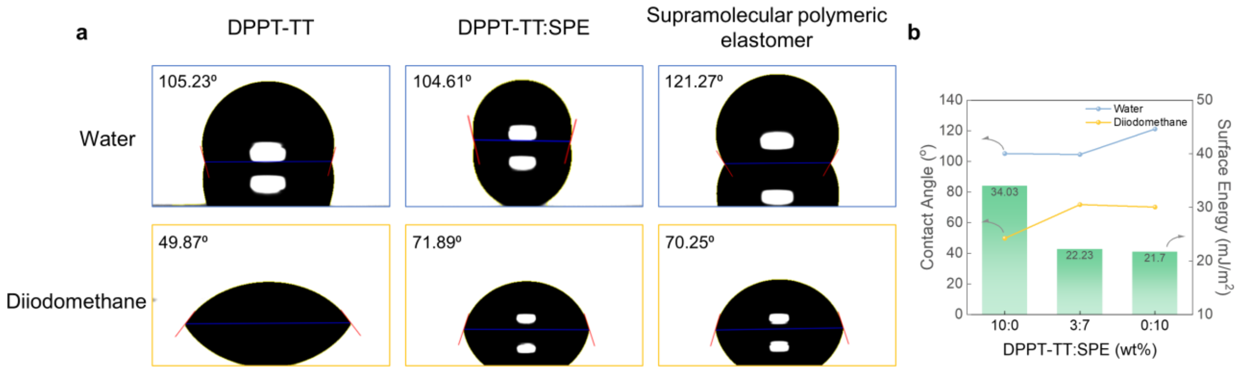

Supplementary Fig. 12. a, Optical image showing the contact angles of the DPPT-TT, 3:7 blending film and supramolecular polymeric elastomer. **b,** The surface energies and contact angles of different films.

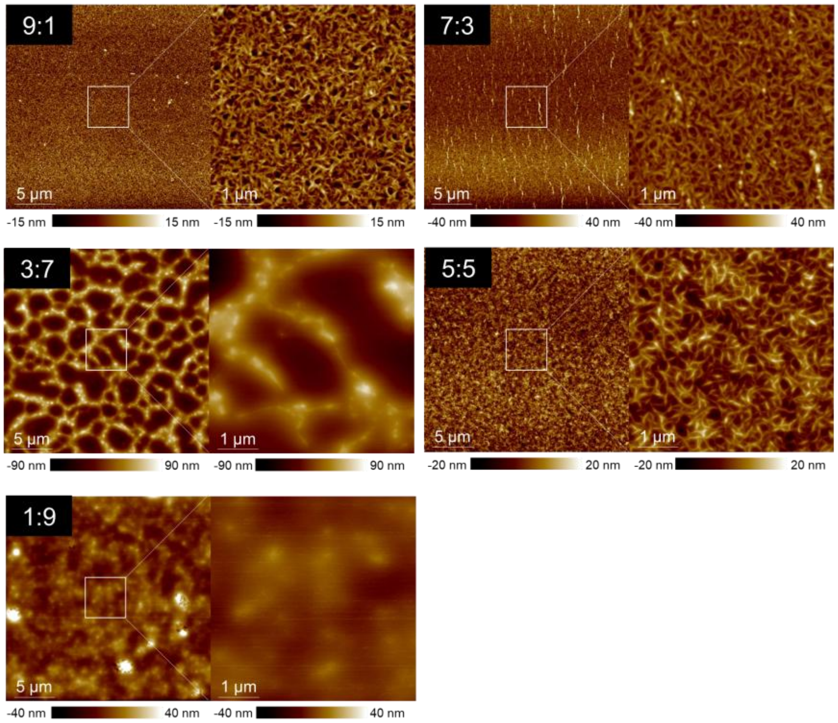

Supplementary Fig. 13. AFM images of DPPT-TT:SPE blending films with various blending ratios. The left images of each ratio are 25×25 μm^2 and right images of each ratio are 5×5 μm^2 scales.

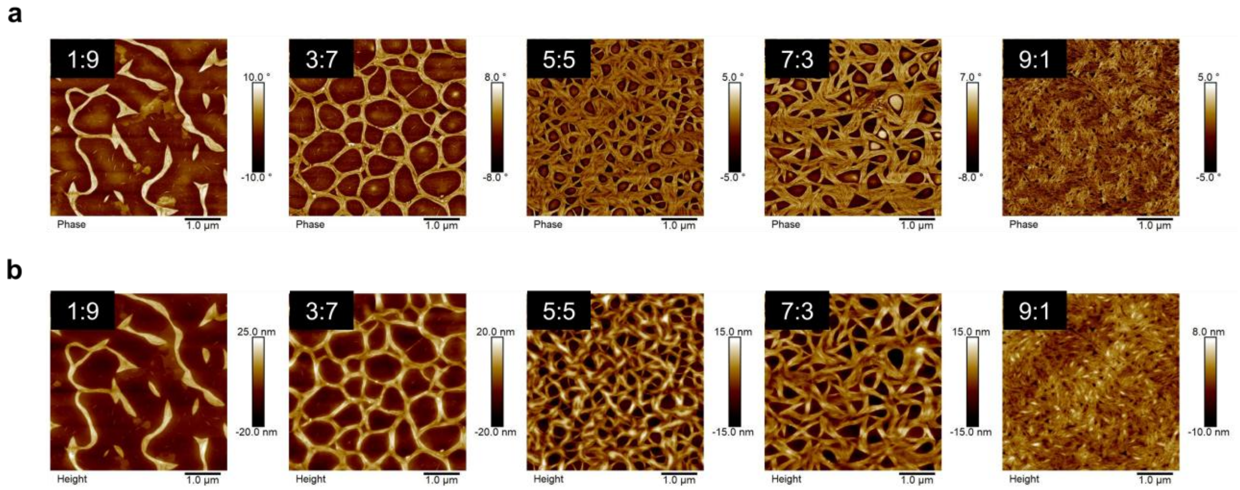

Supplementary Fig. 14. AFM **a,** phase and **b,** height images of N2200:SPE blending films with various blending ratios.

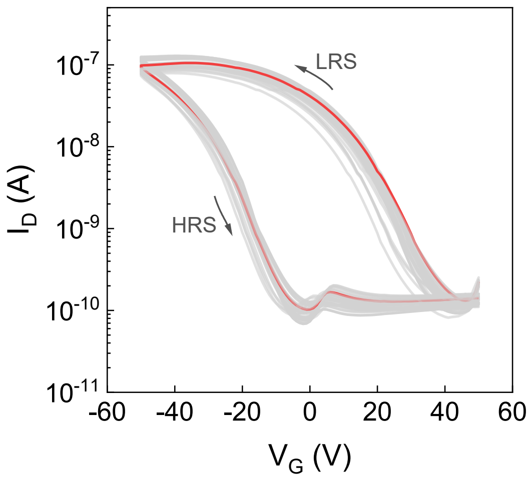

Supplementary Fig. 15. Hysteresis measurement of 49 transistor devices in memtransistor array with gate voltage sweep. V_D = -10 V.

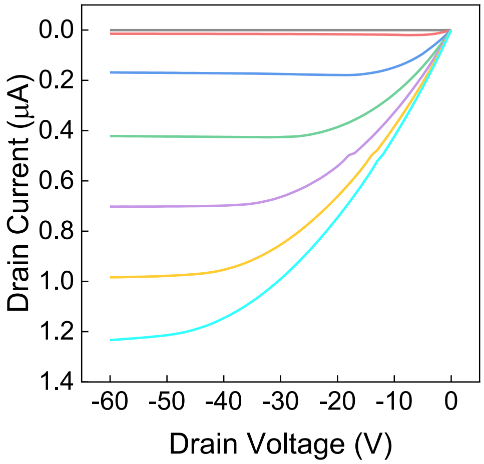

Supplementary Fig. 16. Representative output curve of memtransistor device.

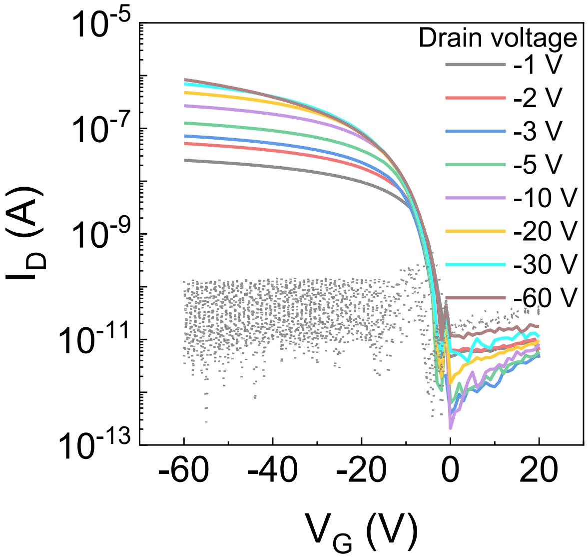

Supplementary Fig. 17. Transfer characteristics of memtransistor device with various drain voltage.

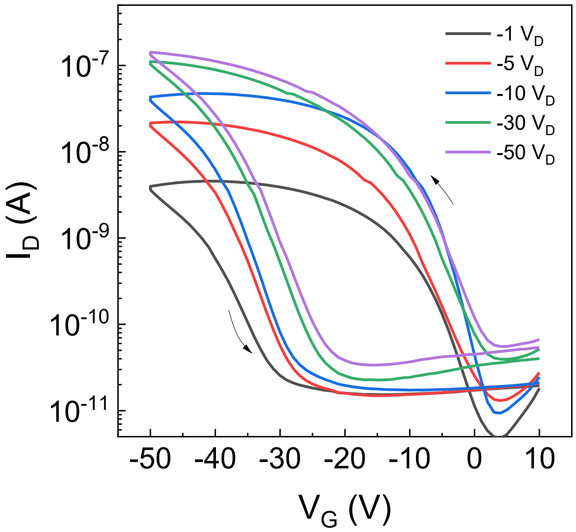

Supplementary Fig. 18. Hysteresis measurement of memtransistor device with various drain voltage.

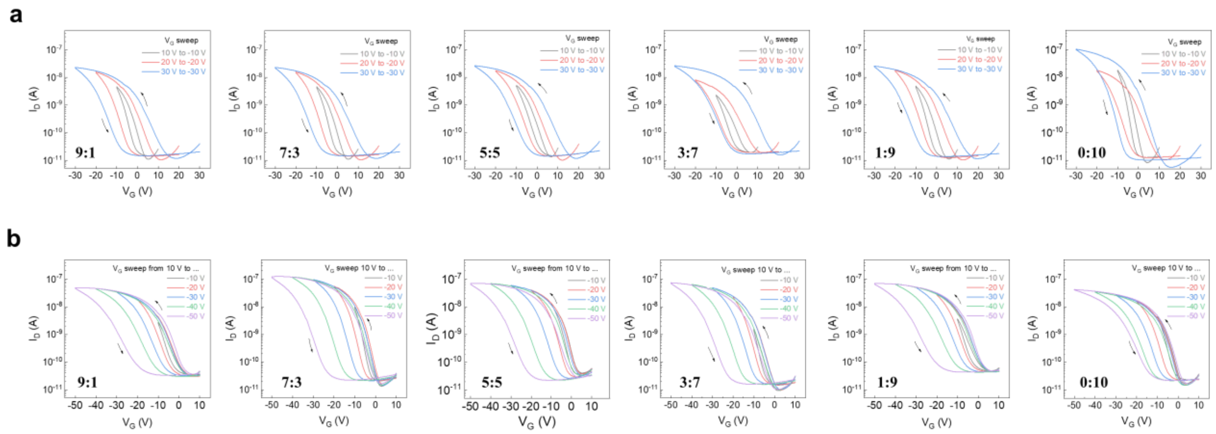

Supplementary Fig. 19. Hysteresis change with different **a,** gate voltage sweep and **b,** negative gate voltage sweep with various weight ratio of N2200 and SPE (N2200:SPE). V_D = 10 V.

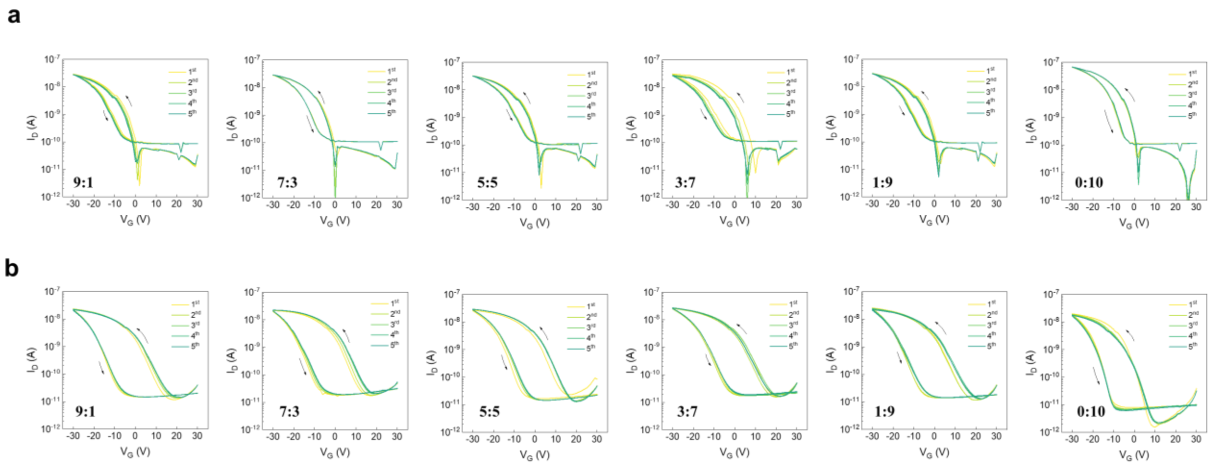

Supplementary Fig. 20. Hysteresis change with 5 consecutive **a,** fast and **b,** slow voltage sweep with various weight ratio of N2200 and SPE (N2200:SPE). V_D = 10 V.

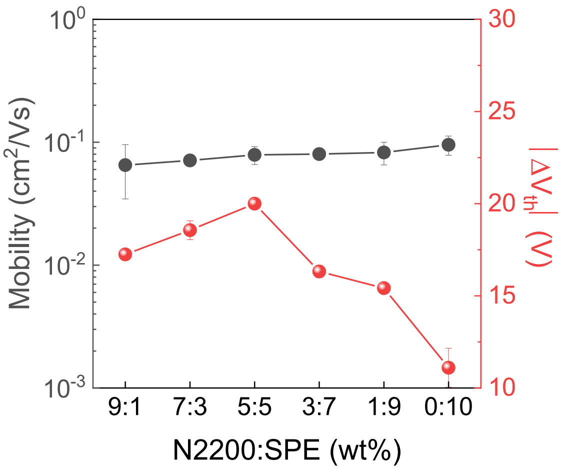

Supplementary Fig. 21. Mobility and shift of threshold voltage change with various ratio of N2200 and SPE. V_D = -10 V. $\Delta|V_{th}| = V_{th\_off} - V_{th\_on}$

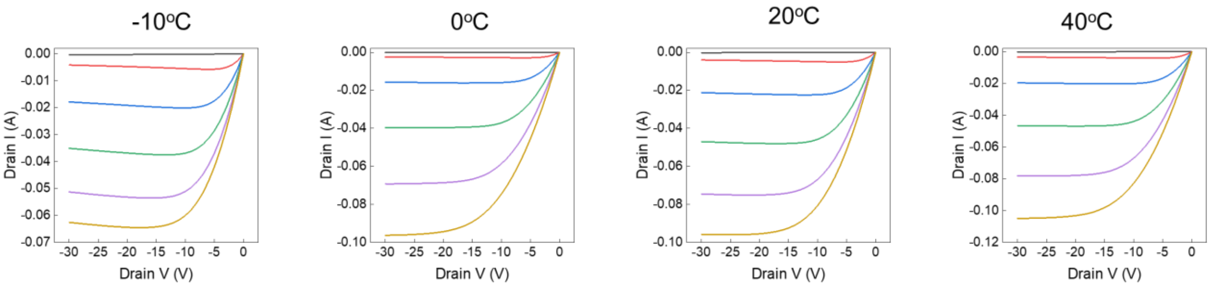

Supplementary Fig. 22. Output characteristics of memtransistor device with various temperature. $V_G = 0 \sim -30$ V, step 10 V.

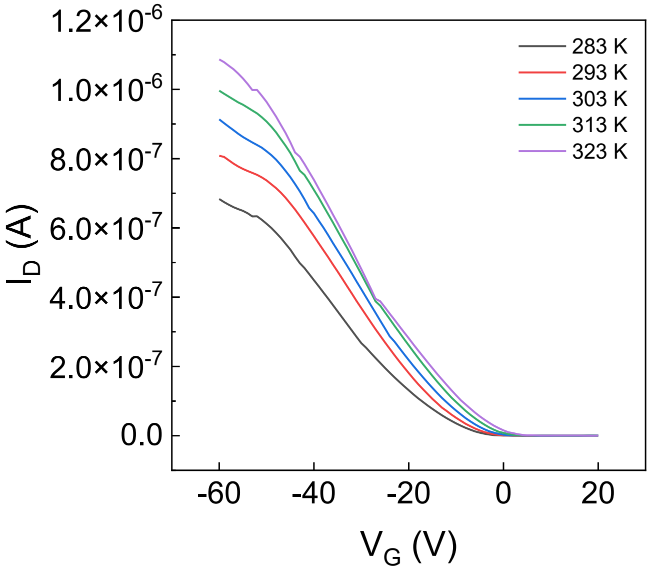

Supplementary Fig. 23. Temperature-dependent transfer characteristics of dual-layer semiconducting films. V_D = -2 V.

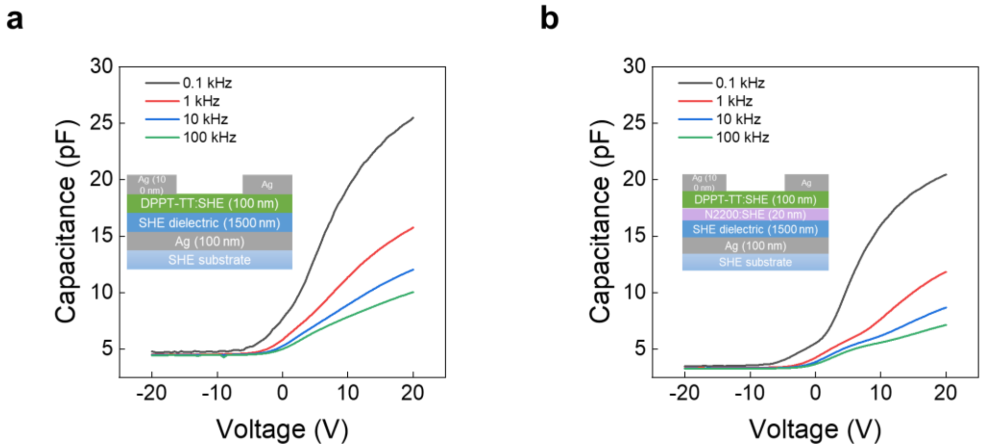

Supplementary Fig. 24. CV curve of **a,** without and **b,** trapping layer with different frequency.

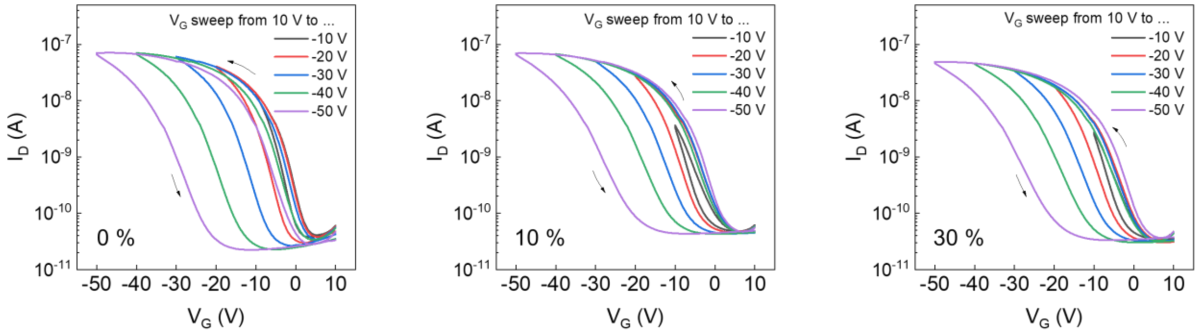

Supplementary Fig. 25. Hysteresis measurement of memtransistor device with various gate voltage sweep under different uniaxial strain. V_D = -10 V.

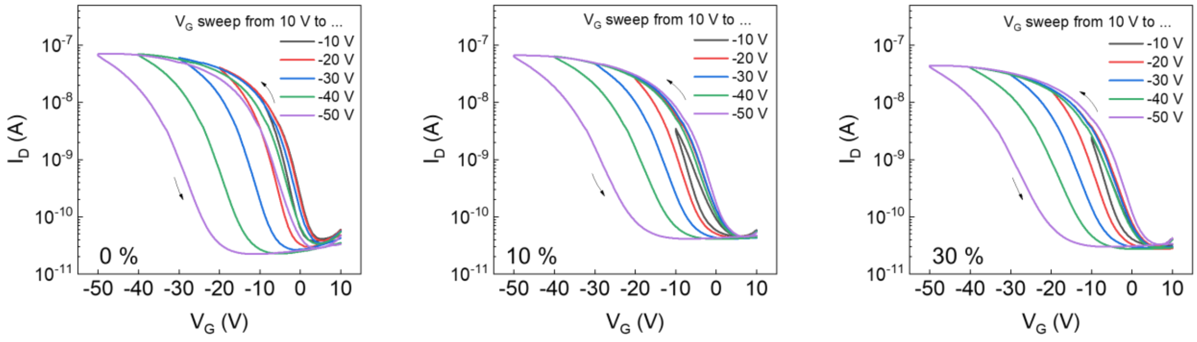

Supplementary Fig. 26. Hysteresis measurement of memtransistor device with various gate voltage sweep under different biaxial strain. V_D = -10 V.

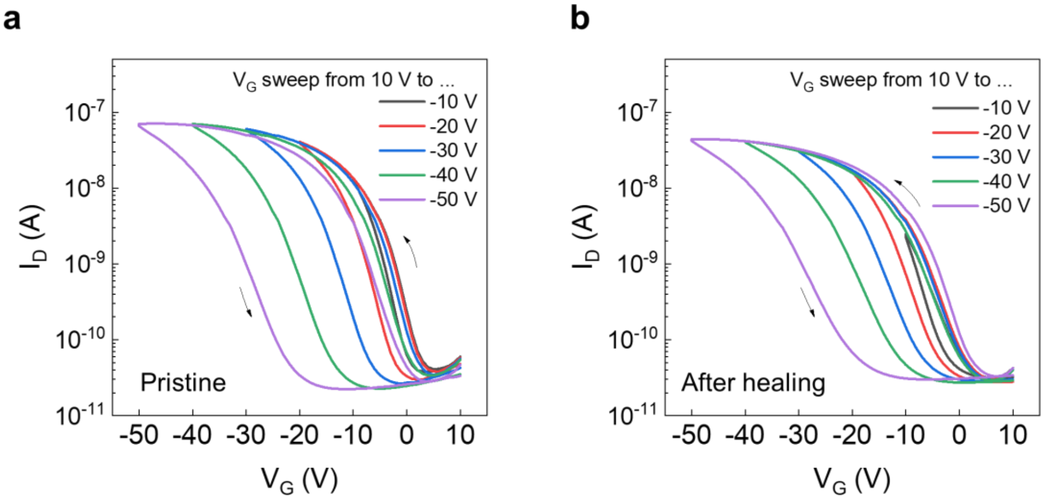

Supplementary Fig. 27. Hysteresis measurement of **a,** pristine and **b,** healed memtransistor device with various gate voltage sweep. V_D = -10 V.

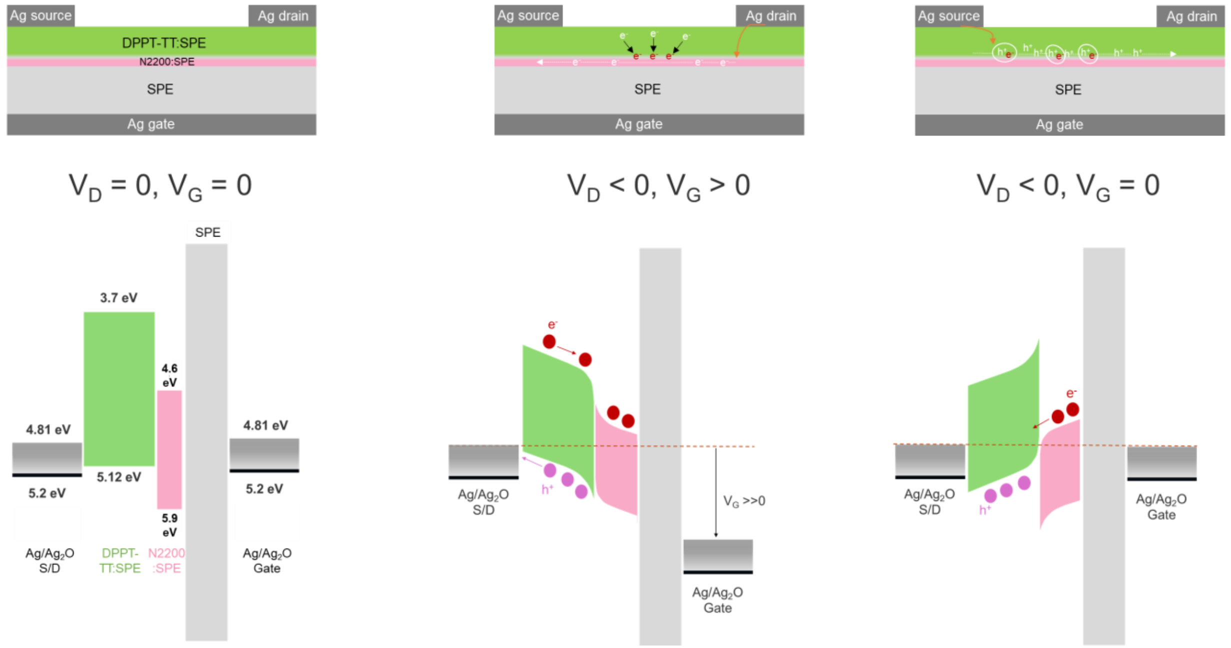

Supplementary Fig. 28. Working mechanism for short term plasticity effect in transistor device. When the device is applied with V_G, holes accumulate at the interface between the semiconductor and the insulating layer. This causes the energy level of the semiconductor to bend, reducing the ϕ_S between the source and the semiconductor. The electrons are trapped by the interface with n-type layer, leading to a higher hole concentration in the p-type channel and increased output current. After the electrical pulse ends, the trapped electrons in n-type layer are compensated by the holes in the channel, resulting in a gradual decrease in the output current for the phenomenon of short-term plasticity effect. Depending on the gate bias, different concentrations of charges are injected into the active layer, enriching the carrier dynamics. The electrical sequence signal can be mapped to different reservoir state spaces by different carrier dynamics, so that its spatiotemporal characteristics can be effectively separated and distributed reservoir states can be realized.

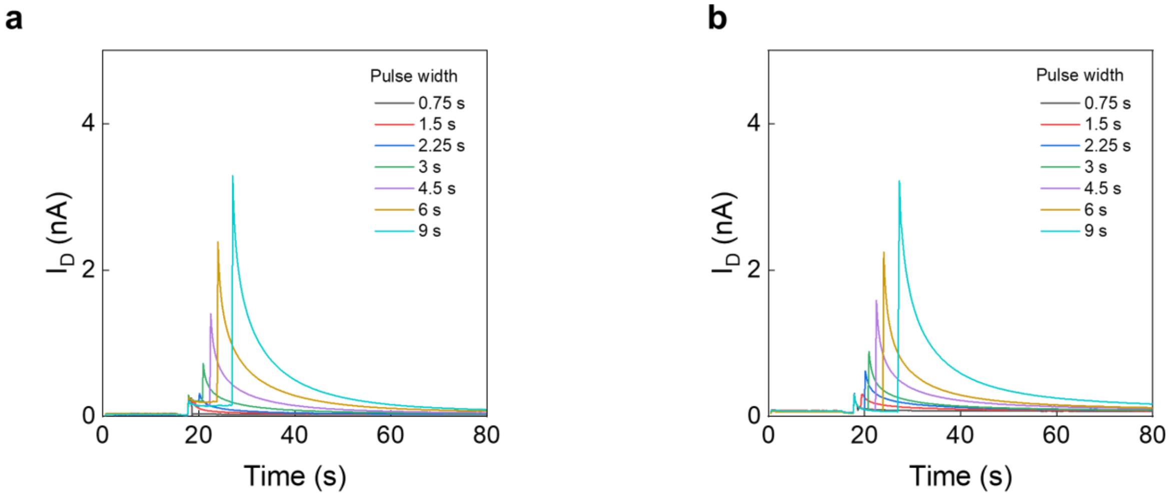

Supplementary Fig. 29. EPSC change of transistor device under **a,** 10 % and **b,** 30 % uniaxial strain with different pulse width. V_D = -1 V.

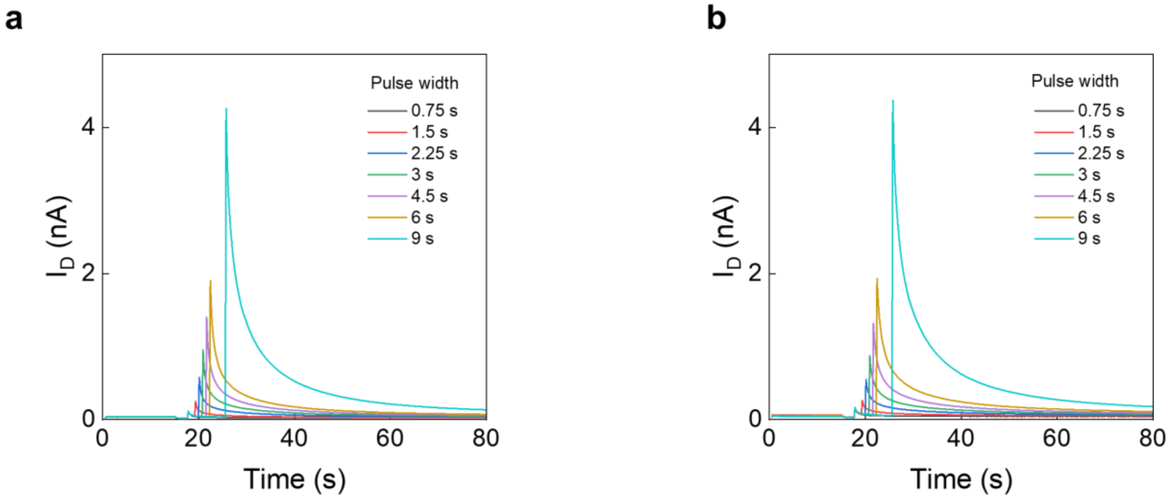

Supplementary Fig. 30. EPSC change of transistor device under **a,** 10 % and **b,** 30 % biaxial strain with different pulse width. V_D = -1 V.

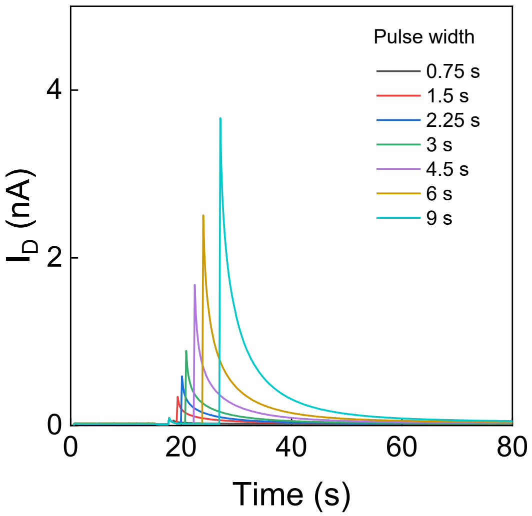

Supplementary Fig. 31. EPSC change of transistor device after healing with different pulse width. $V_D = -1$ V.

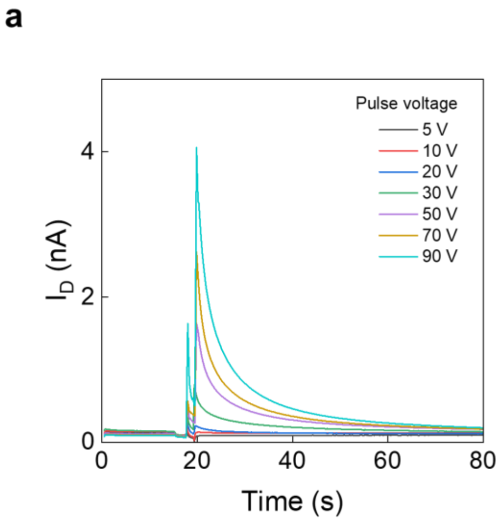

Supplementary Fig. 32. EPSC change of transistor device under **a,** 10 % and **b,** 30 % uniaxial strain with different pulse voltage. V_D = -1 V.

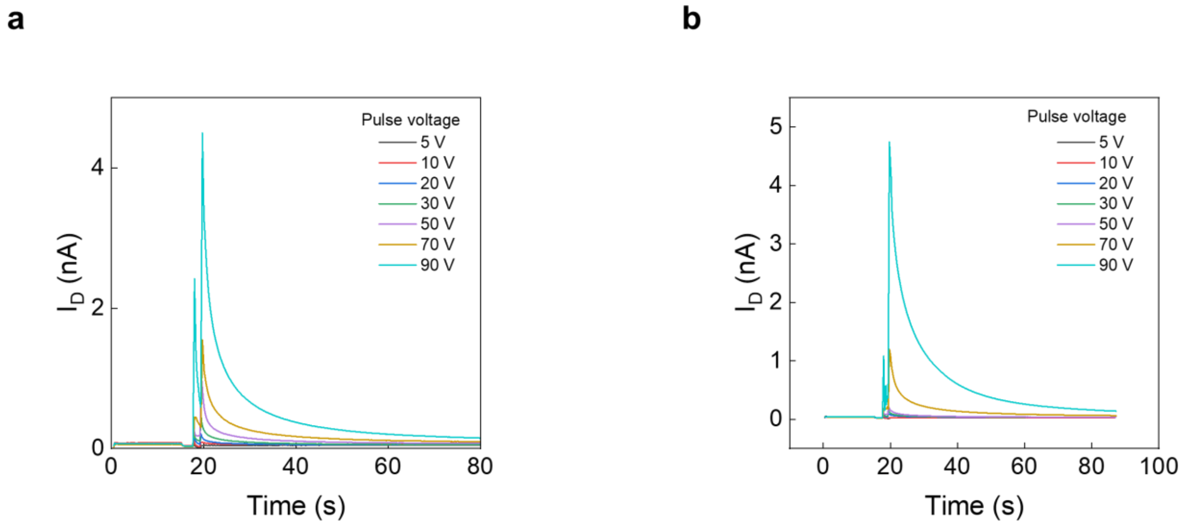

Supplementary Fig. 33. EPSC change of transistor device under **a,** 10 % and **b,** 30 % biaxial strain with different pulse voltage. V_D = -1 V.

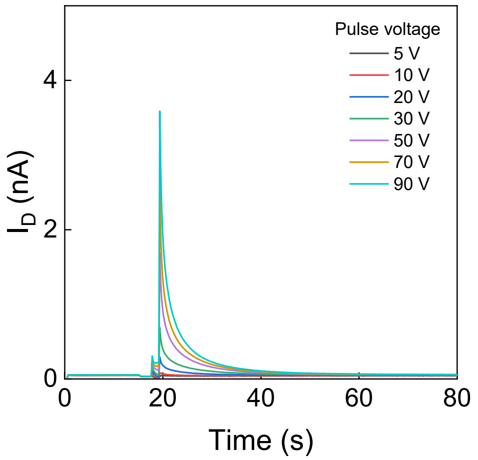

Supplementary Fig. 34. EPSC change of transistor device after healing with different pulse voltage. V_D = -1 V.

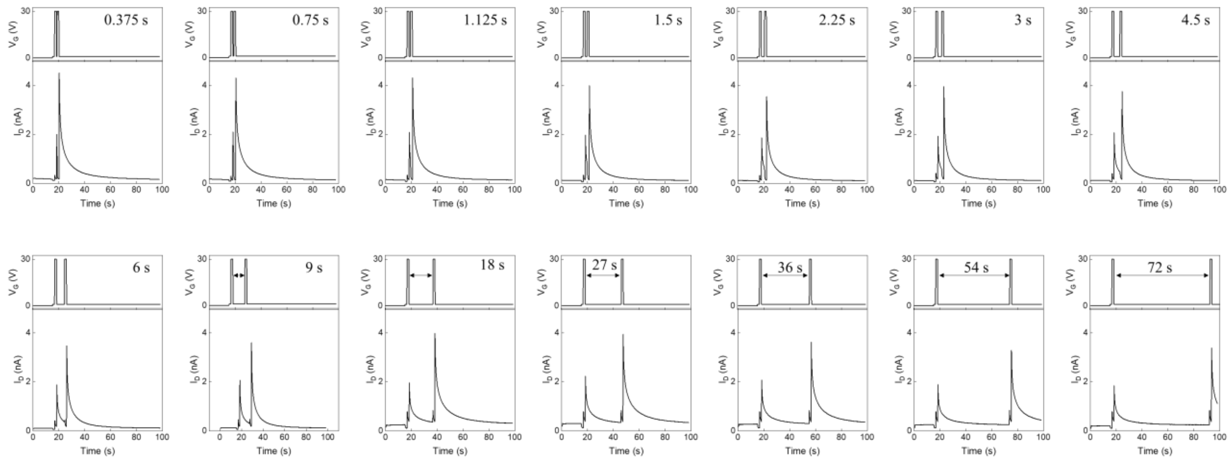

Supplementary Fig. 35. EPSC change of pristine device under two pulses with different interval time (0.375 sec - 72 sec). V_D = -1 V.

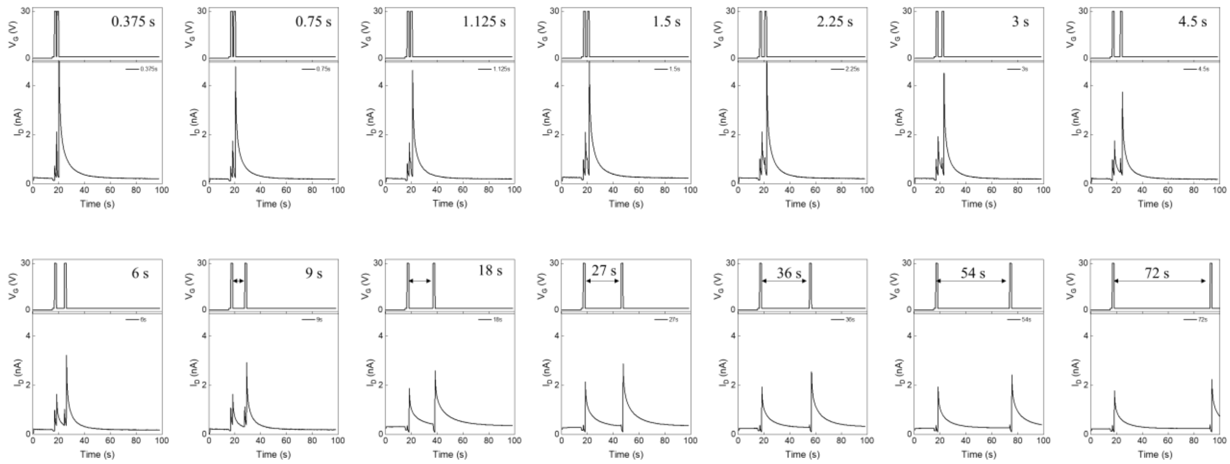

Supplementary Fig. 36. EPSC change of 30 % uniaxially stretched device under two pulses with different interval time (0.375 sec - 72 sec). V_D = -1 V.

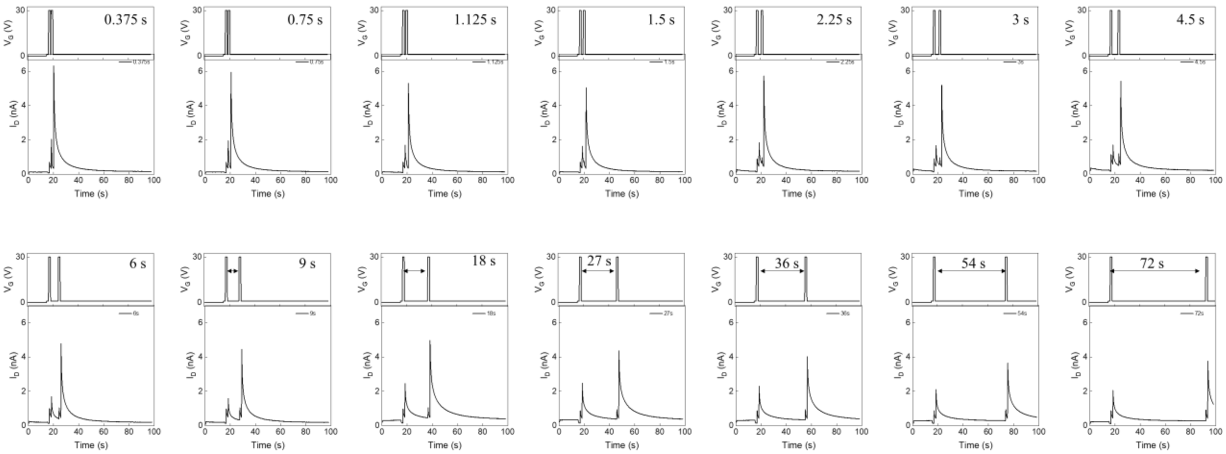

Supplementary Fig. 37. EPSC change of 30 % biaxially stretched device under two pulses with different interval time (0.375 sec - 72 sec). V_D = -1 V.

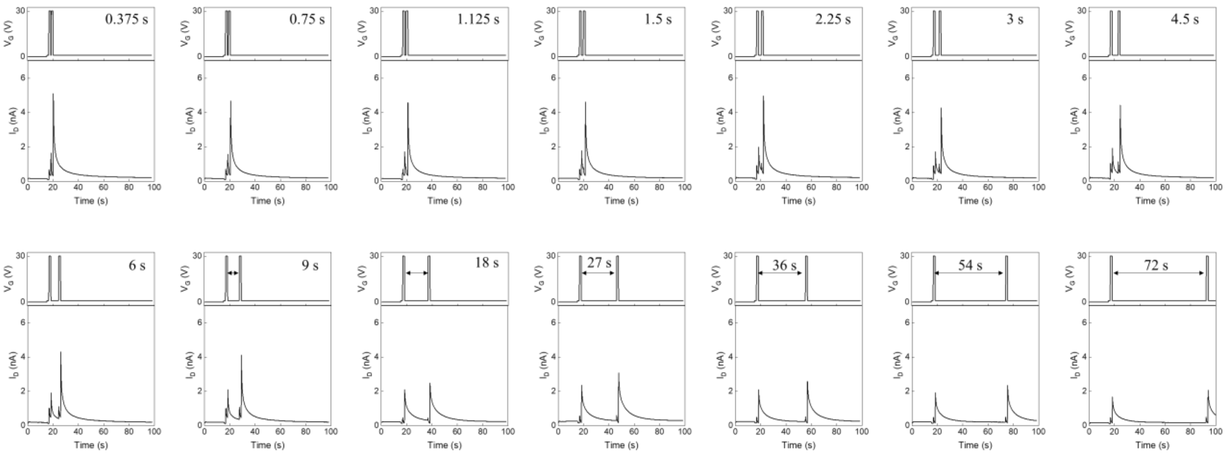

Supplementary Fig. 38. EPSC change of healed device under two pulses with different interval time (0.375 sec - 72 sec). V_D = -1 V.

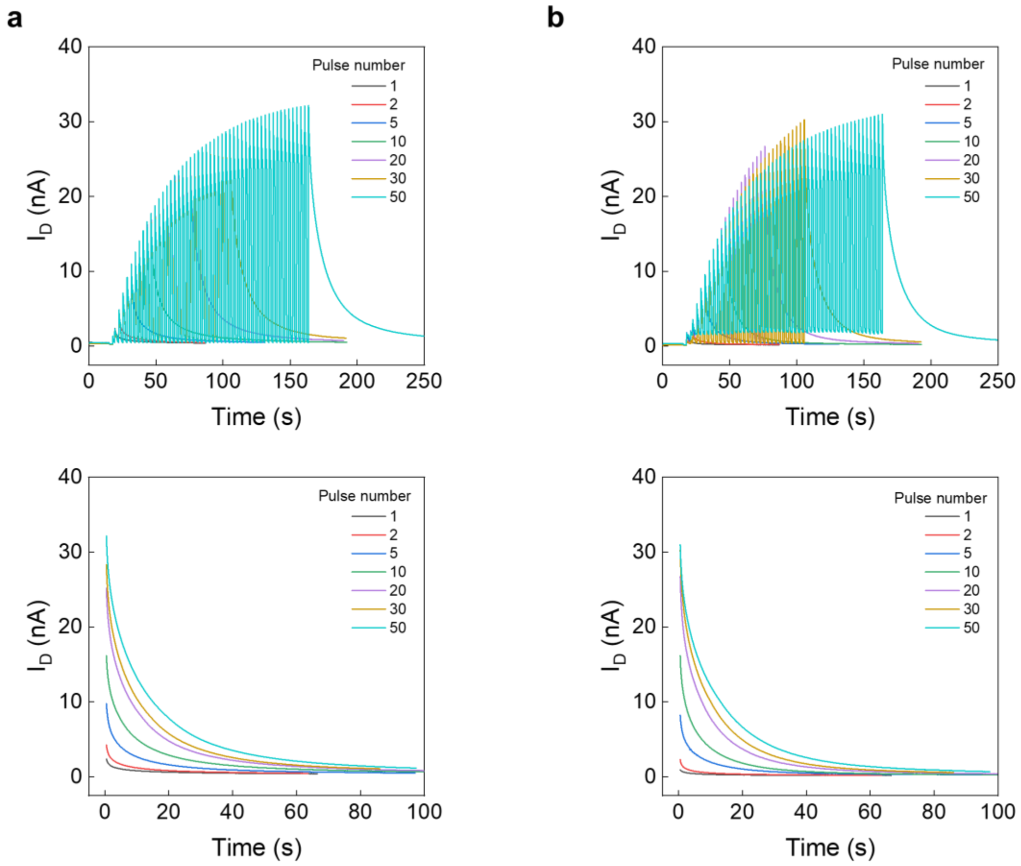

Supplementary Fig. 39. EPSC (top) and decay current (bottom) change of transistor device under **a,** 10 % and **b,** 30 % uniaxial strain with different pulse number. $V_D = -1$ V.

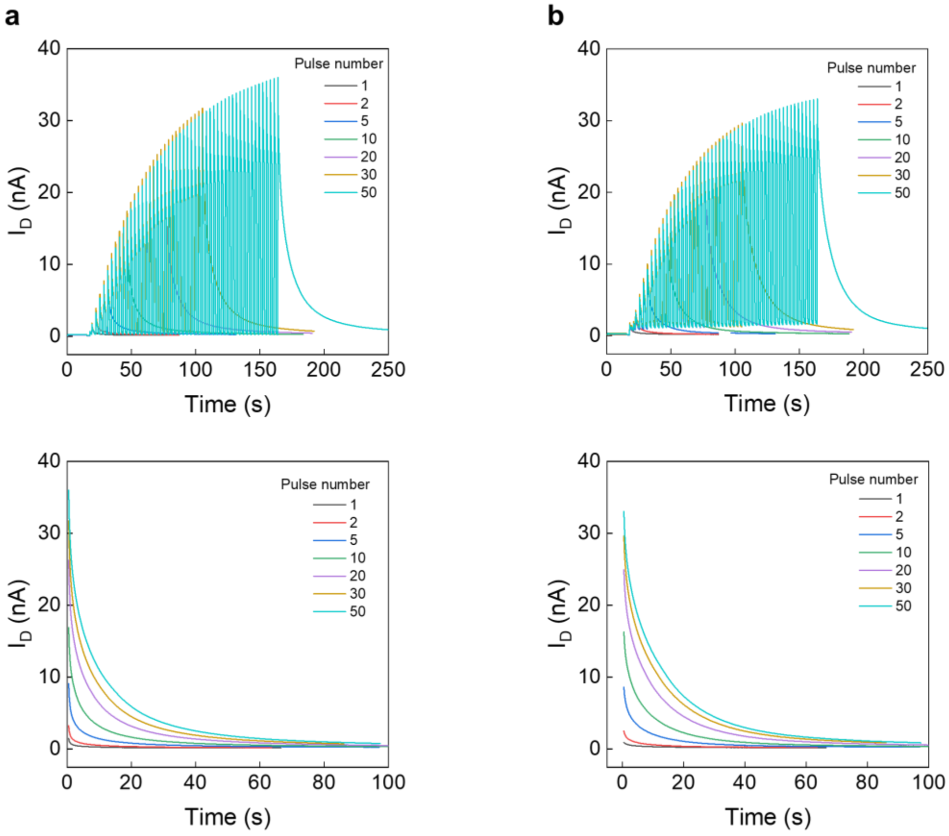

Supplementary Fig. 40. EPSC (top) and decay current (bottom) change of transistor device under **a,** 10 % and **b,** 30 % biaxial strain with different pulse number. $V_D = -1$ V.

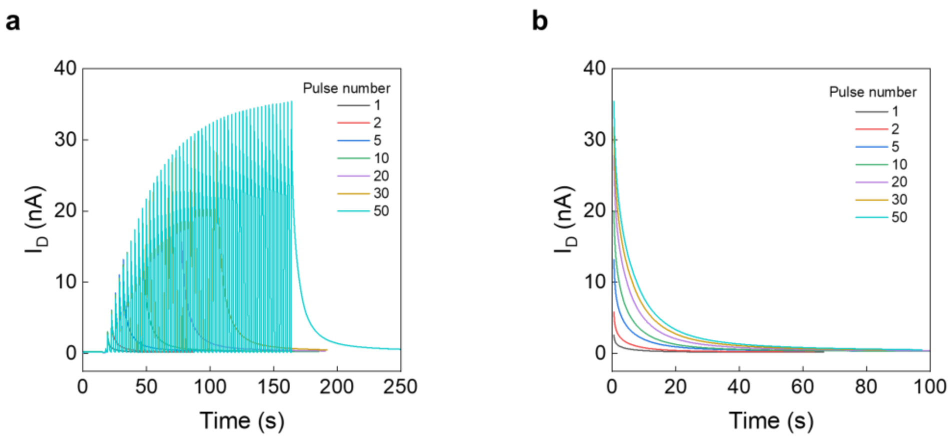

Supplementary Fig. 41. a, EPSC and **b,** decay current change of transistor device after healing with different pulse number. V_D = -1 V.

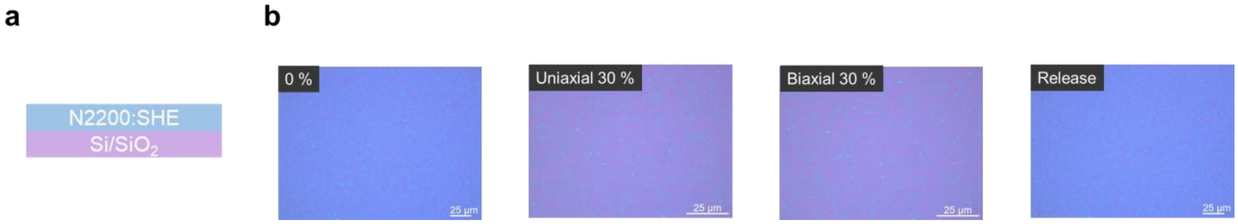

Supplementary Fig. 42. a, Schematic structure of blend n-type semiconducting films for stretchability. **b,** Optical images of n-type films with tensile strain.

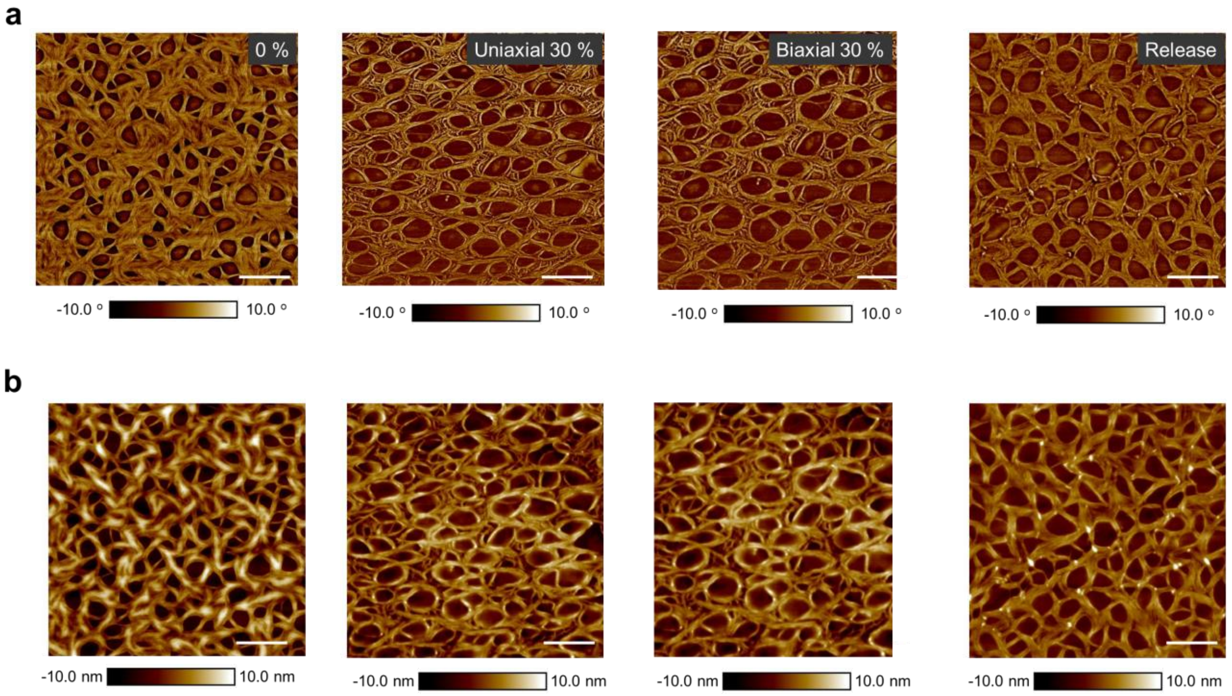

Supplementary Fig. 43. AFM **a,** phase and **b,** height images of blend n-type semiconducting films for stretchability test. Scale bar: 1.0 µm.

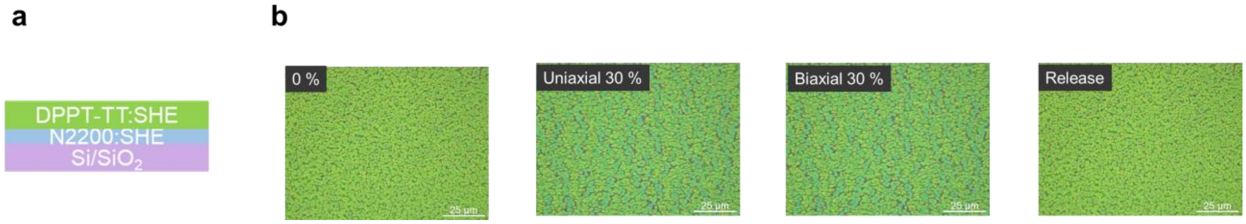

Supplementary Fig. 44. a, Schematic structure of dual layer films for stretchability. **b,** Optical images of dual layer films with tensile strain.

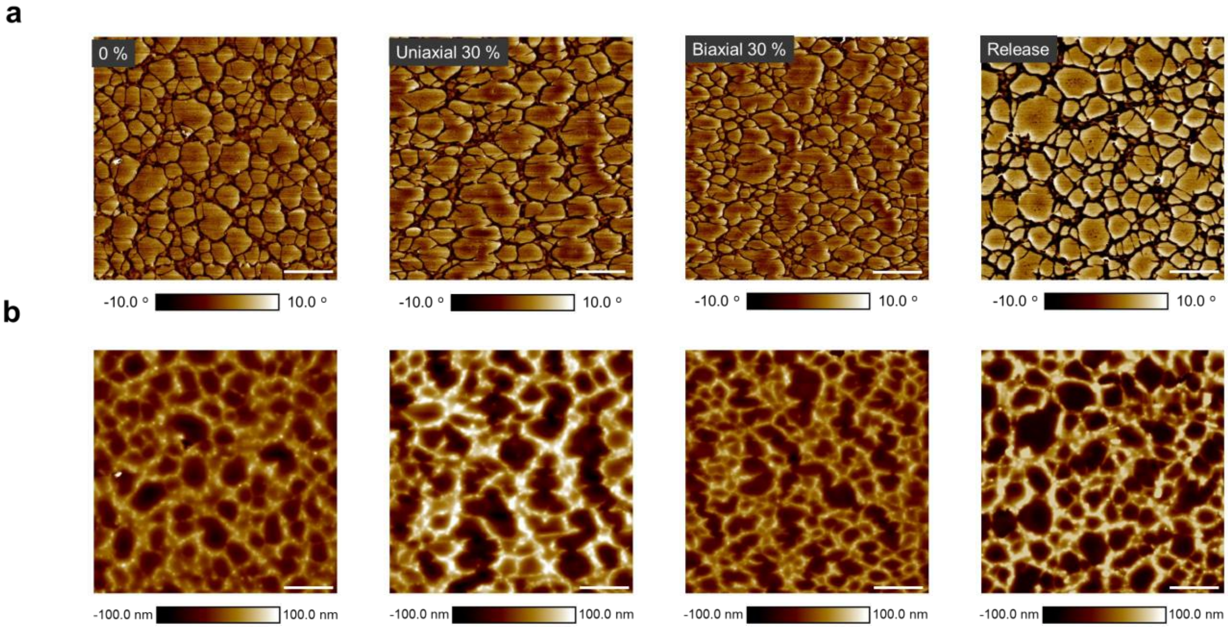

Supplementary Fig. 45. AFM **a,** phase and **b,** height images of dual layer films for stretchability test. Scale bar: 5.0 µm.

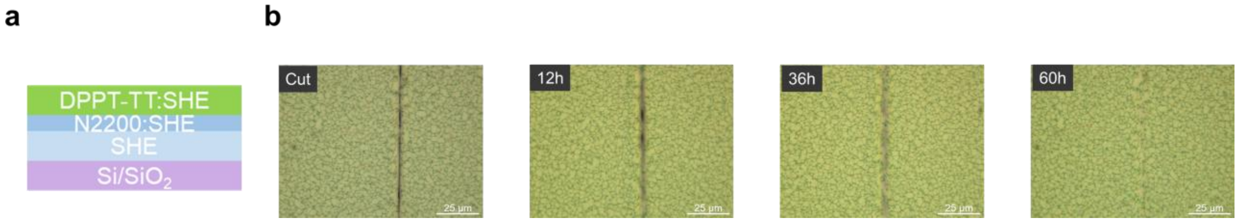

Supplementary Fig. 46. a, Schematic structure of dual layer films for tracking healing time. **b,** Optical images of dual layer films with healing time.

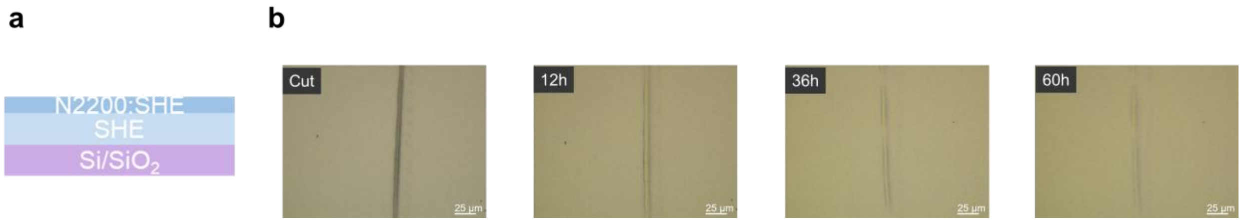

Supplementary Fig. 47. a, Schematic structure of blend n-type films for tracking healing time. **b,** Optical images of dual layer films with healing time.

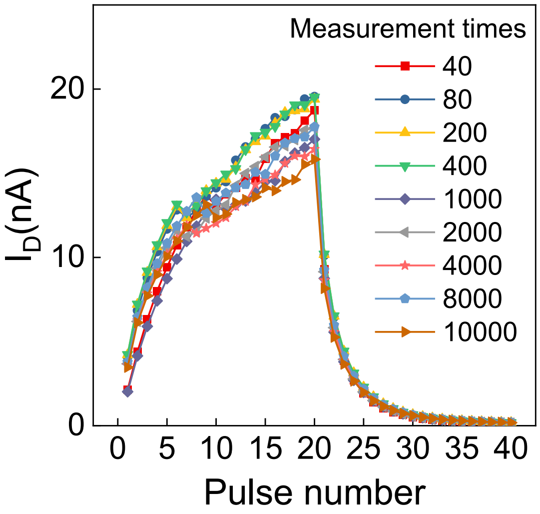

Supplementary Fig. 48. Endurance test of transistor devices up to 10000 pulses (20 pulse with 40 V, t_{pre} 3 s, 20 pulse with −0.5 V, t_{pre} 3 s).

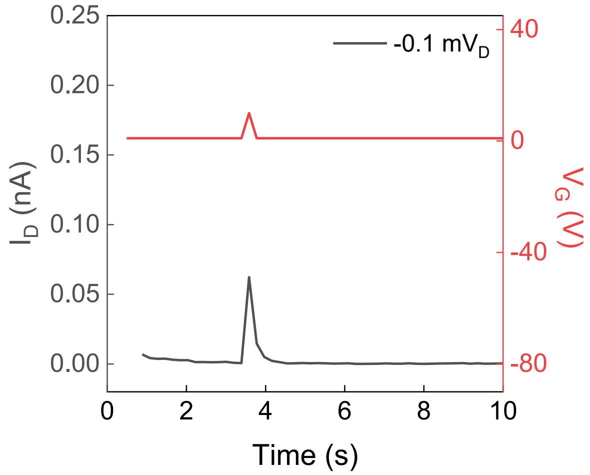

Supplementary Fig. 49. Drain current in low drain voltage operation to calculate power consumption ($V_{G,pulse}$ 10 V, t_{pre} 0.2 s, V_D -0.1 mV). Power consumption is defined by: $E_c = I_{EPSC} \times V_D \times t_{pulse}$, where I_{EPSC} is the peak value of EPSC, V_D is the drain voltage, and t_{pulse} is the duration of gate pulse, reducing the values of these three factors is effective for achieving low energy consumption.

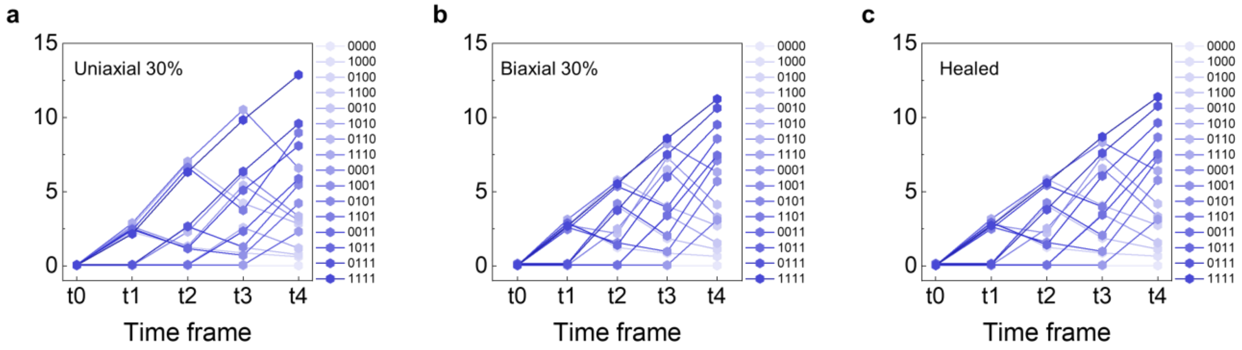

Supplementary Fig. 50. Change in reservoir states performance with various device state: **a,** 30% uniaxial stretching, **b,** 30% biaxial stretching, **c,** healed. The measurements were performed with V_{pulse} = 40 V for “1”, V_{read} = 1 V for “0”, and t_{pulse} = 3 s.

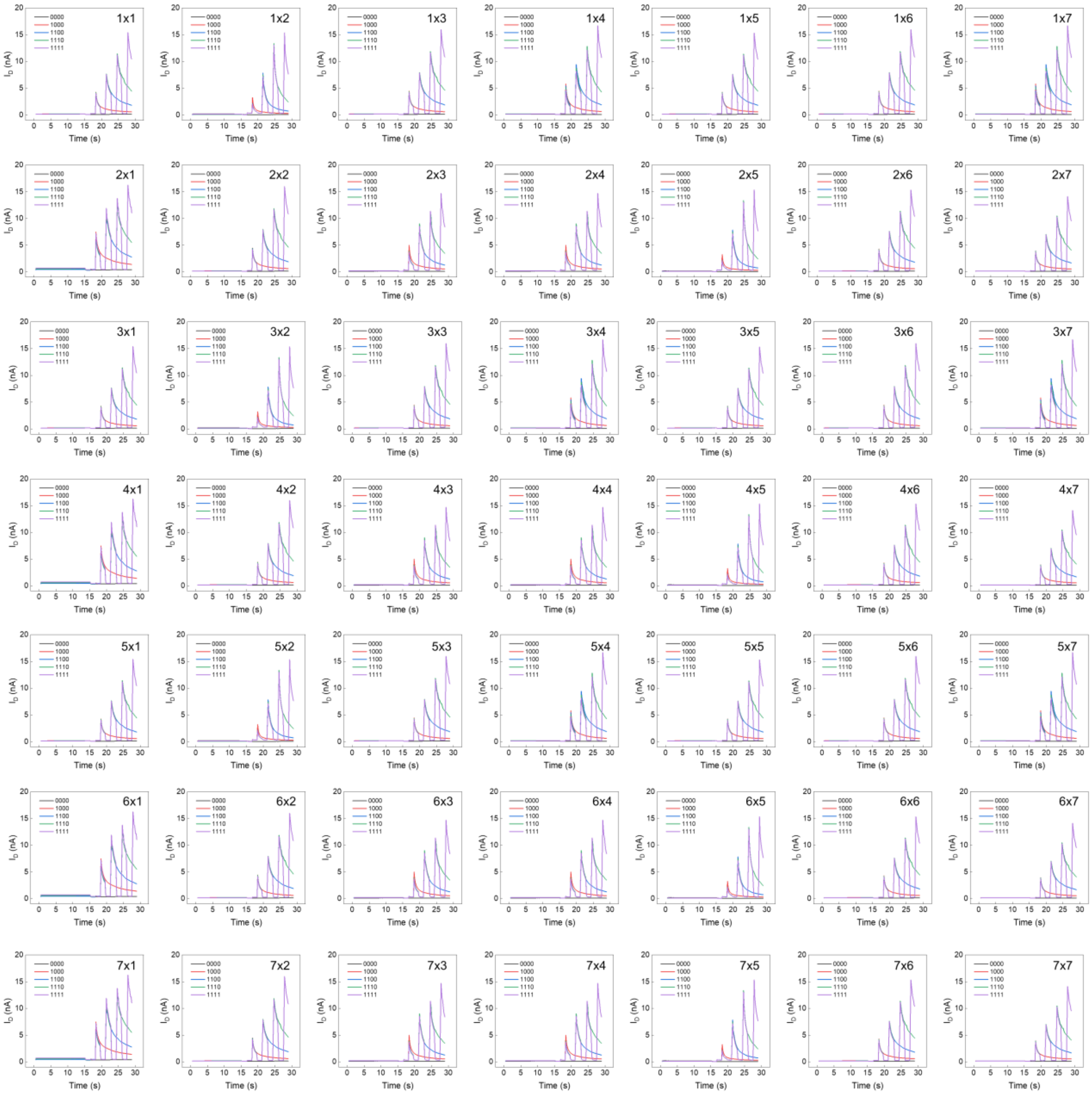

Supplementary Fig. 51. Drain current change in reservoir performance of 7x7 active matrix array with various electrical pulses (V_{pulse} = 40 V, V_{read} = 1 V, t_{pulse} = 3 s). The results demonstrate that all devices in the array exhibit minimal variation, confirming their high uniformity.

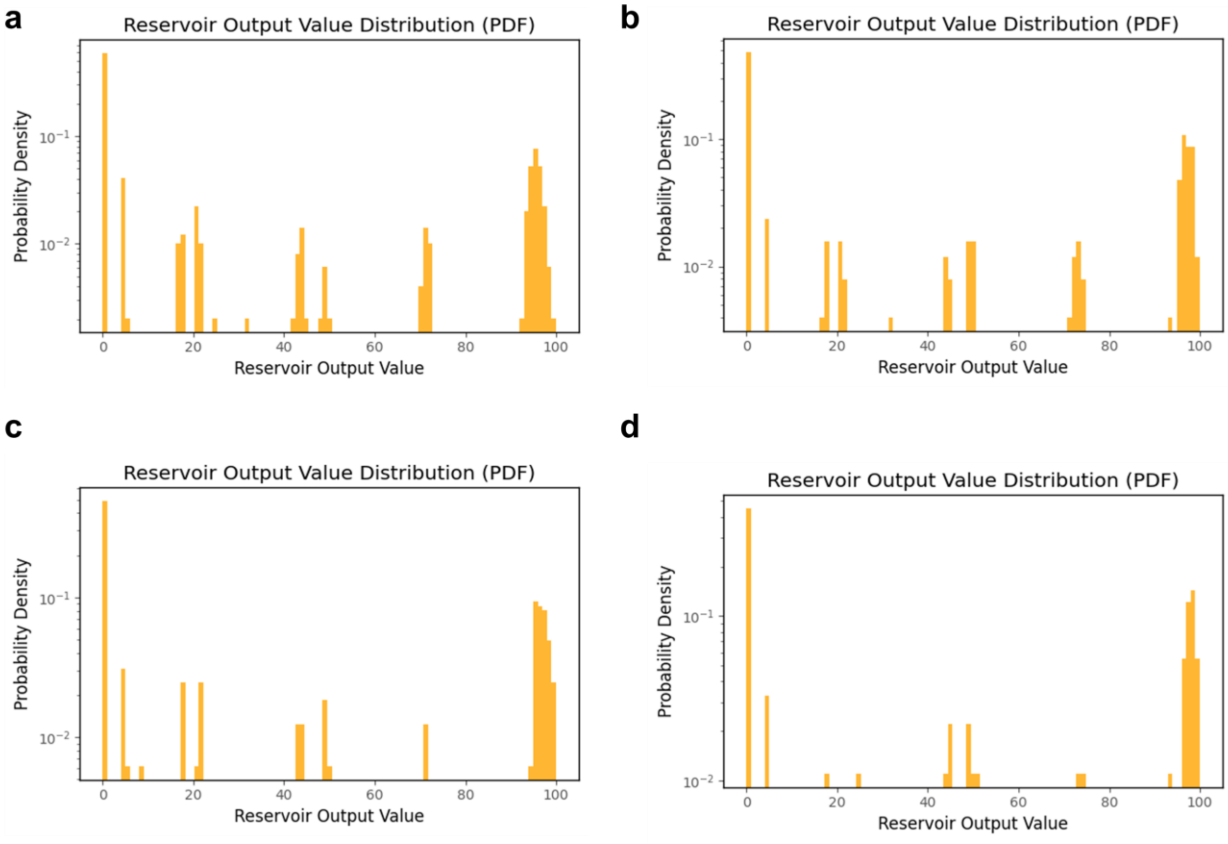

Supplementary Fig. 52. a, Probability density function (PDF) of Audio-MNIST data projected into the high-dimensional feature map via the reservoir with 49 channels, **b,** 25 channels, **c,** 16 channels, and **d,** 9 channels.

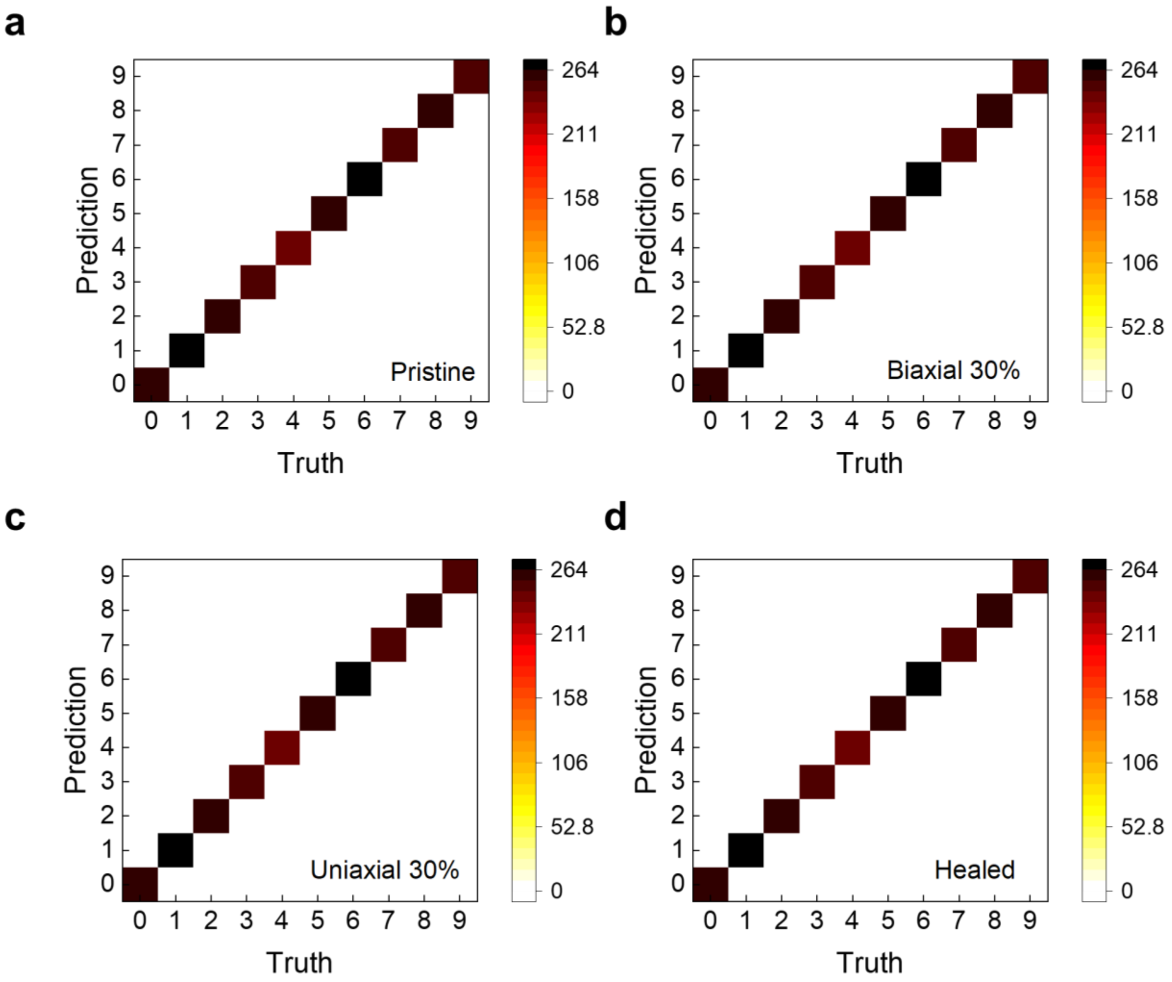

Supplementary Fig. 53. a, Confusion matrix of the pristine device for AudioMNIST. **b,** Confusion matrix of the uniaxial device for AudioMNIST. **c,** Confusion matrix of the biaxial device for AudioMNIST. **d,** Confusion matrix of the healed device for AudioMNIST.

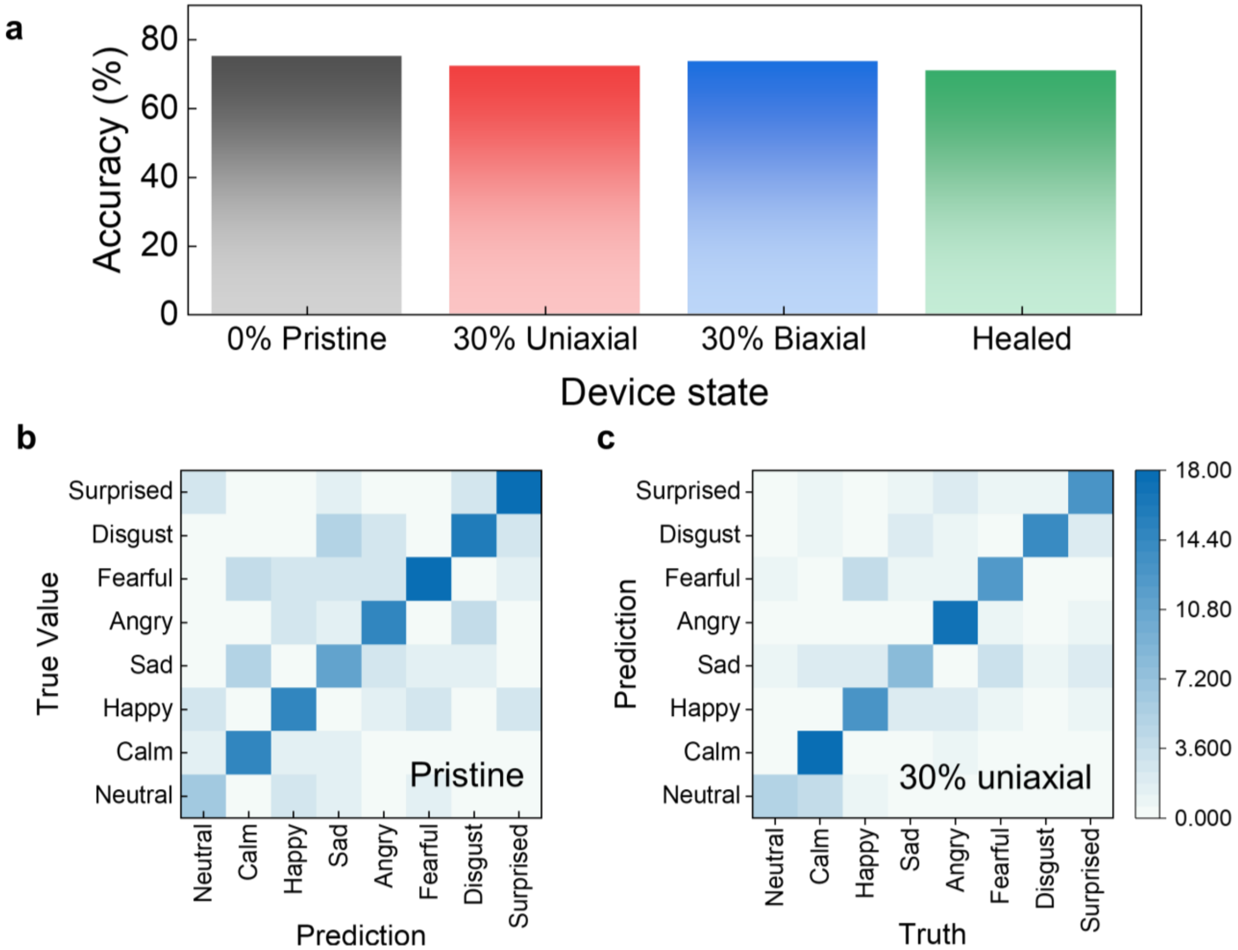

Supplementary Fig. 54. a, Accuracy for the various device states for RAVDESS with various device states. **b,** Confusion matrix of the pristine device with variation for RAVDESS **c,** Confusion matrix of the uniaxial device with variation for RAVDESS.

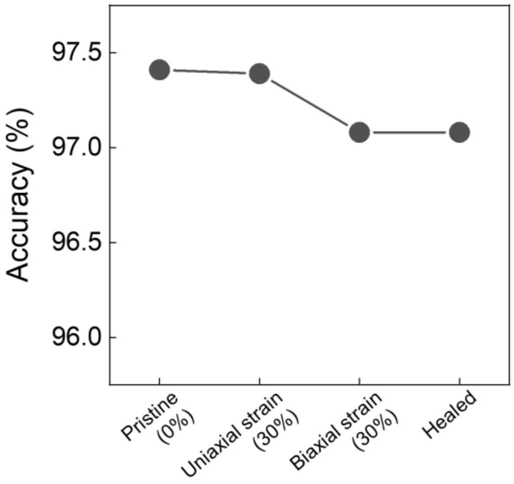

Supplementary Fig. 55. Accuracy for the various device states for MNIST with various device states.

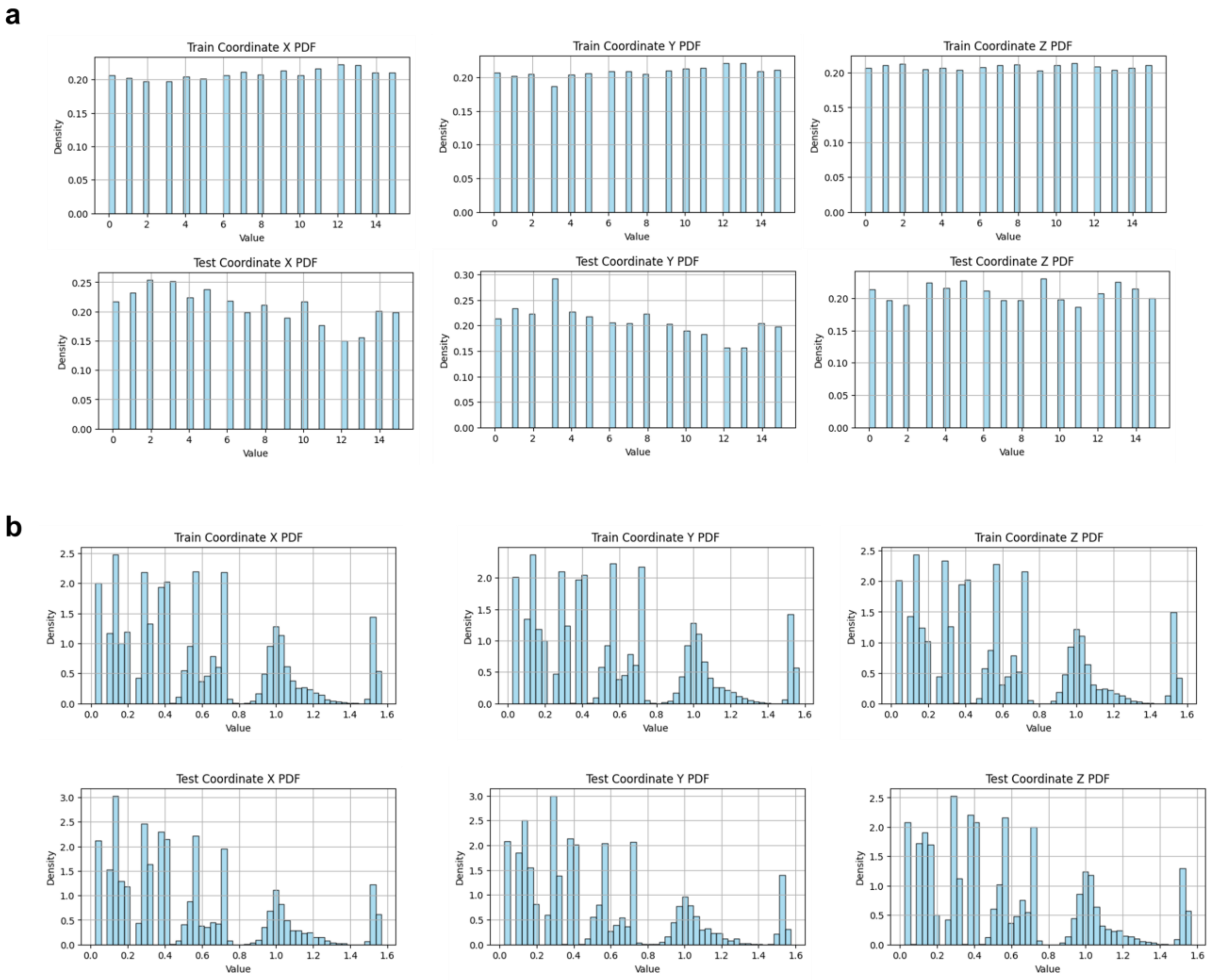

Supplementary Fig. 56. a, PDF of the original Lorenz attractor coordinates for each axis **b,** PDF of the Lorenz attractor coordinates after passing through the reservoir, for each axis.

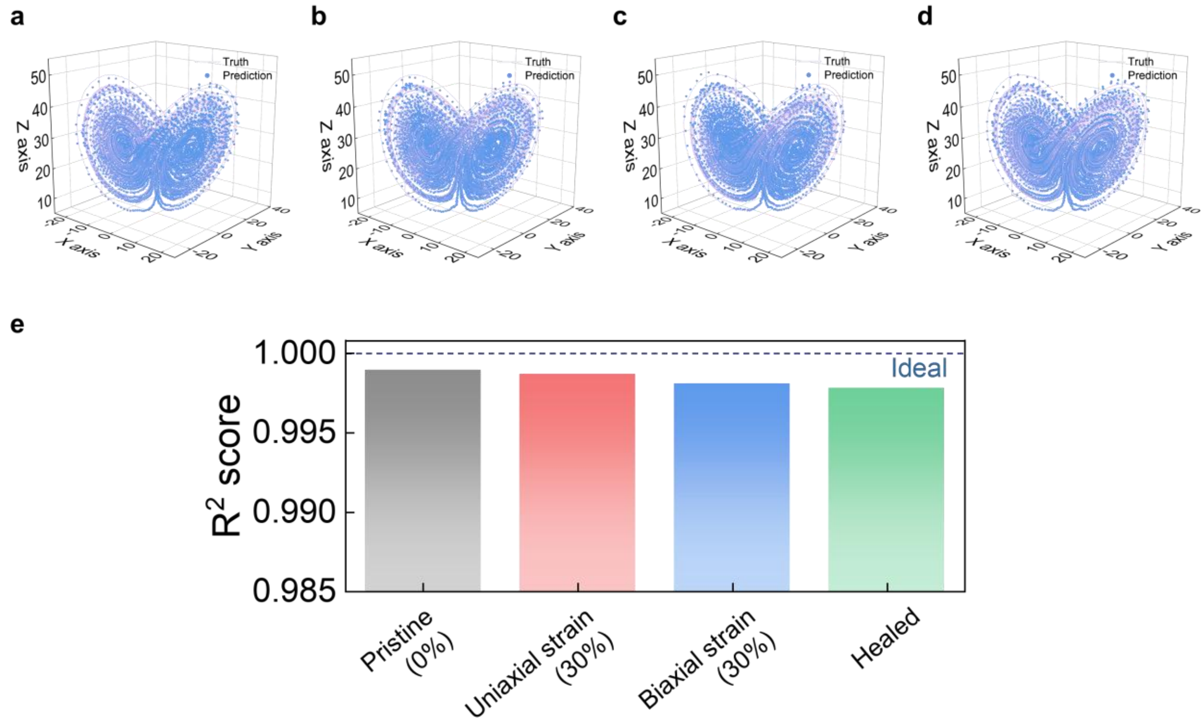

Supplementary Fig. 57. 3D-plot of the **a,** pristine **b,** uniaxial **c,** biaxial **d,** healed device for Lorenz attractor with the one-step ahead method **e,** the R^2 score for the various device states for Lorenz attractor. The pristine, uniaxial, biaxial, and healed devices have R2 scores of 0.99893, 0.9987, 0.99809, and 0.9978, respectively.

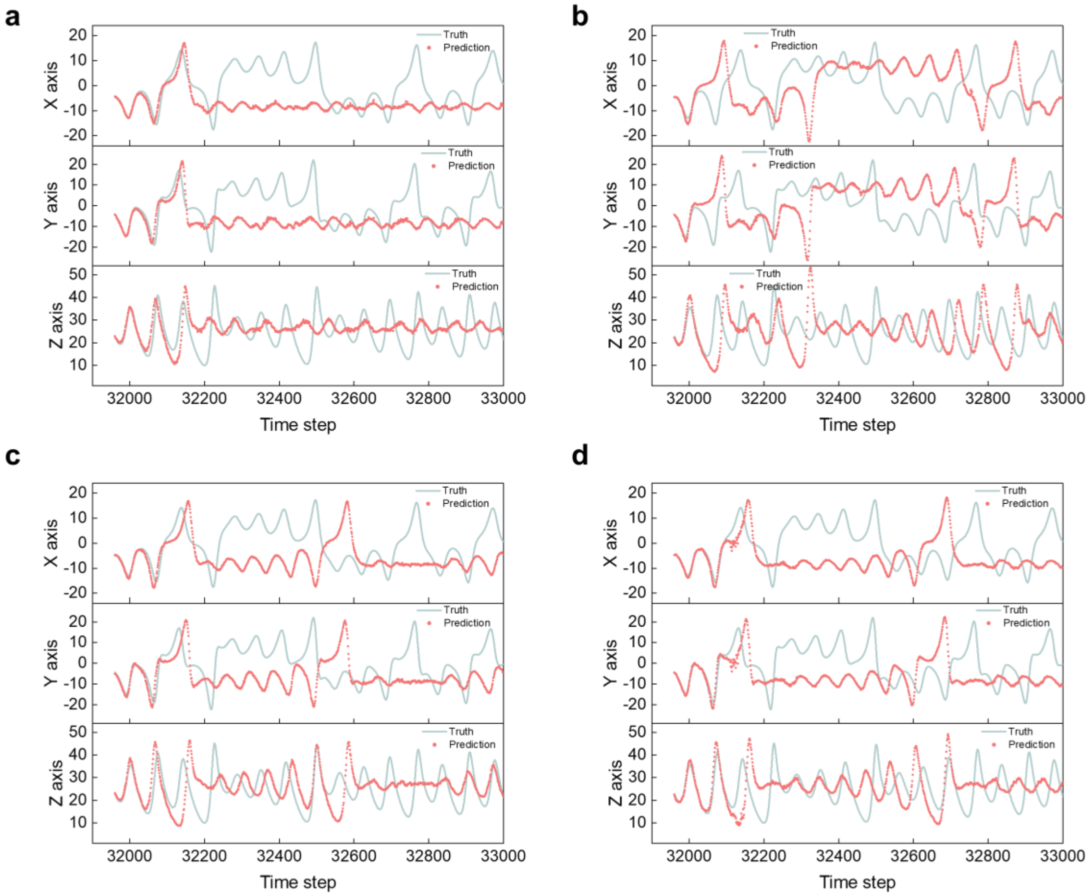

Supplementary Fig. 58. 1D-plot of the **a,** pristine **b,** uniaxial **c,** biaxial **d,** healed device for Lorenz attractor with the recursive multi-step ahead method.

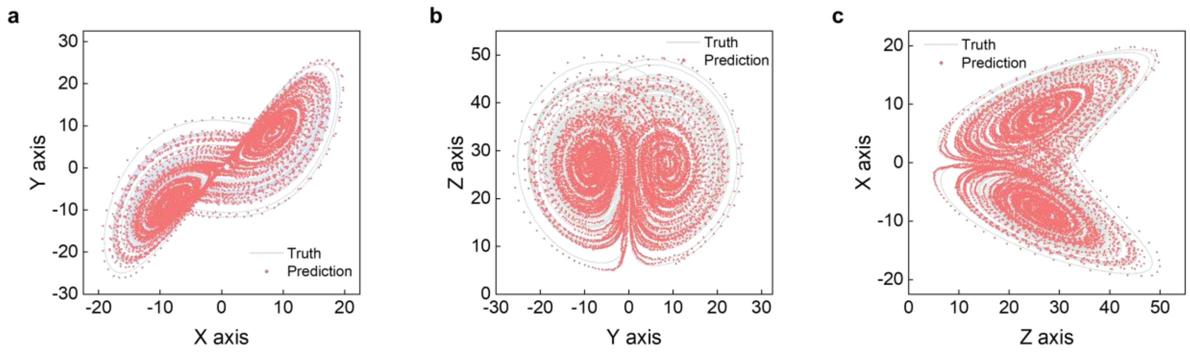

Supplementary Fig. 59. 2D-projections of the predicted Lorenz Attractor coordinates on the **a,** X-Y **b,** Y-Z **c,** Z-X planes, obtained using the pristine device trained online.

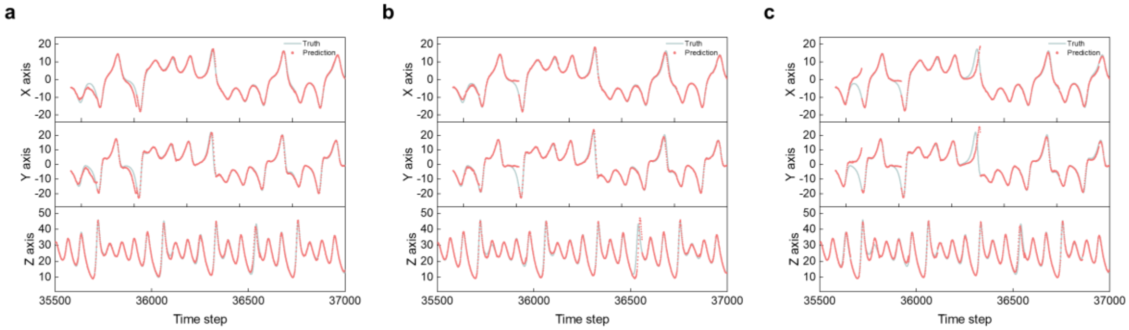

Supplementary Fig. 60. 1D-trajectory of the predicted Lorenz Attractor obtained using the **a,** uniaxial, **b,** biaxial and **c,** healed device trained online.

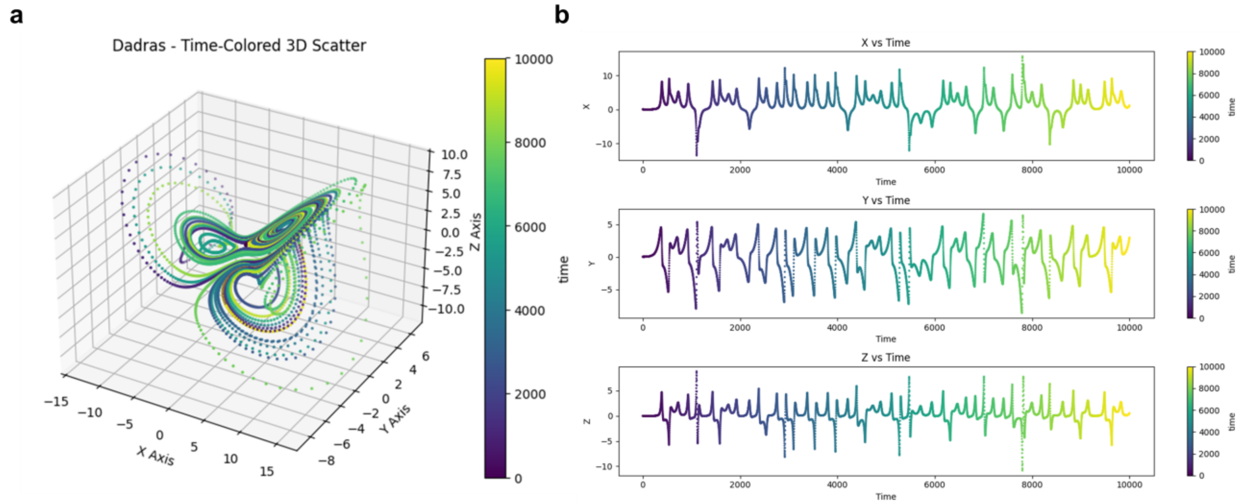

Supplementary Fig. 61. a, Representative plots of the Dadras attractor: three-dimensional trajectory and **b,** one-dimensional time series.

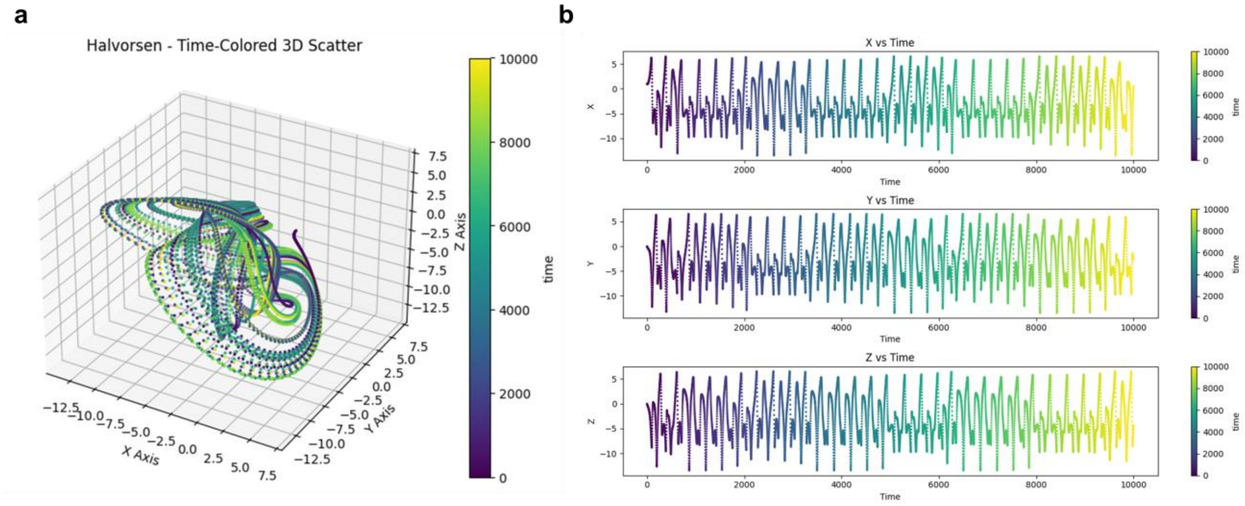

Supplementary Fig. 62. a, Representative plots of the Halvorsen attractor: three-dimensional trajectory and **b,** one-dimensional time series.

Supplementary Tables

Supplementary Table 1. Device geometry and dielectric capacitance under strain.

Stretching	Strain (%)	Channel length (µm)	Channel width (µm)	Capacitance (nF/cm^2)
Uniaxial (ll)	0	150	1000	1.75
	10	176	918	1.80
	20	193	883	1.88
	30	202	857	1.9
Uniaxial (=)	0	150	1000	1.75
	10	137	1180	1.85
	20	132	1180	1.85
	30	130	1257	1.93
Biaxial (×)	0	150	1000	1.75
	10	176	1032	1.86
	20	188	1092	1.94
	30	199	1148	2.24

Note that the capacitance values of gate dielectric were obtained at 1 kHz.

Supplementary Table 2. Comparison of our performance and previously reported works.

Device type	Active layer	Stimuli signal	τ value range	Reservoir states	Energy consumption	Stretchability	Healing ability	Ref.
OFET	DPPT-TT:SPE, N2200:SPE	Electrical	1 – 5	16	0.29 fJ – 1.8 nJ	Uniaxial: 30% Biaxial: 30%	All components	This work
OFET	P0FDIID: N2200	Electrical, light	0.005 – 13.2	1152	N/A	N/A	N/A	[3]
OFET	p-NDI	Light	0.01 – 2.1	32	N/A	Flexible	N/A	[4]
FFET	$Hf_{0.5}Zr_{0.5}O_2$	Electrical	26.9 – 275.9	16	<1μW	N/A	N/A	[5]
FFET	$HZO/TiN/ZrO_2$	Electrical	30 – 50	32	N/A	N/A	N/A	[6]
FFET	HfO_2	Electrical	N/A	32	0.2 pJ	N/A	N/A	[7]
FFET	$Hf_{0.5}Zr_{0.5}O_2$	Electrical	N/A	16	35 pJ	N/A	N/A	[9]
OECT	PTBT-p	Electrical	0.05	16	3.6 pJ	N/A	N/A	[10]
OECT	PTBT-p	Electrical	N/A	32	<1μW	Flexible	N/A	[11]

*OFET: Organic field effect transistor. FFET: Ferroelectric field effect transistor. OECT: Organic electrochemical transistor. N/A: Not applicable.

References

1. Owens, D. K. et al. Estimation of the surface free energy of polymers. *J. Appl. Polym. Sci.* **13**, 1741–1747 (1969).
2. Gao, C. et al. Toward grouped-reservoir computing: organic neuromorphic vertical transistor with distributed reservoir states for efficient recognition and prediction. *Nat. Comm.* **15**, 740 (2024).
3. Wu, X., Wang, S. et al. Wearable in-sensor reservoir computing using optoelectronic polymers with through-space charge-transport characteristics for multi-task learning. *Nat. Comm.* **14**, 468 (2023).
4. Du, C. et al. Reservoir computing using dynamic memristors for temporal information processing. *Nat. Comm.* **8**, 2204 (2017).
5. Zhong, Y. et al. Dynamic memristor-based reservoir computing for high-efficiency temporal signal processing. *Nat. Comm.* **12**, 408, (2021).
6. Kim, J., Park, E. C., Shin, W. et al. Analog reservoir computing via ferroelectric mixed phase boundary transistors. *Nat. Comm.* **15**, 9147 (2024).
7. Liu, K. et al. An optoelectronic synapse based on α-In_2Se_3 with controllable temporal dynamics for multimode and multiscale reservoir computing. *Nat. Electron.* **5**, 761-773 (2022).
8. Choi, S. et al. 3D-integrated multilayered physical reservoir array for learning and forecasting time-series information. *Nat. Commun.* **15**, 2044 (2024).
9. Liu, Z., Zhang, Q., Xie, D. et al. Interface-type tunable oxygen ion dynamics for physical reservoir computing. *Nat. Commun.* **14**, 7176 (2023).
10. Appeltant, L. et al. Information processing using a single dynamical node as complex system. *Nat. Commun.* **2**, 468 (2011).
11. Wang, S., Chen, X. et al. An organic electrochemical transistor for multi-modal sensing, memory and processing. *Nat. Electron.* **6**, 281-291 (2023).